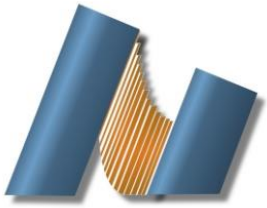

UNIVERSIDAD NACIONAL AUTÓNOMA DE MÉXICO
CENTRO DE NANOCIENCIAS Y NANOTECNOLOGÍA

LICENCIATURA EN NANOTECNOLOGÍA
BIONANOTENOLOGÍA

DESIGN AND CHARACTERIZATION OF MULTIMODALITY P22 BACTERIOPHAGE FOR COMBINATORY THERAPY OF BREAST CANCER

TESIS
QUE PARA OPTAR POR EL TÍTULO DE:
LICENCIADO EN NANOTECNOLOGÍA

PRESENTA:
DANIEL DE JESUS PLIEGO SOSA

DIRECTOR DE TESIS
DRA. KANCHAN CHAUHAN

ENSENADA, BAJA CALIFORNIA. JUNIO 2020.

Hago constar que el trabajo que presento es de mi autoría y que todas las ideas, citas textuales, datos, ilustraciones, gráficas, etc. sacados de cualquier obra o debidas al trabajo de terceros, han sido debidamente identificados y citados en el cuerpo del texto y en la bibliografía y acepto que en caso de no respetar lo anterior puedo ser sujeto de sanciones universitarias.

Afirmo que el material presentado no se encuentra protegido por derechos de autor y me hago responsable de cualquier reclamo relacionado con la violación de derechos de autor.

Daniel de Jesus Pliego Sosa

Abstract

The multifunctionalized nanocarriers have been widely studied as a novel way to fight cancer cells, some of these carriers are used for the controlled and targeted delivery of enzymes, prodrugs, photosensitizers, etc. However, these nanoplatforms are usually designed to perform one specific therapy, and there are few studies reporting a combination of therapies. The main objective of this work is to synthesize P22 viral capsids with GOx-CYP activity and indocyanine green (IcG) covalently bonded to the capsid surface in order to evaluate their use as nanoreactors for combination of enzyme-prodrug, starvation, photodynamic, and photothermal therapies against breast cancer. In the first part, P22-CYP capsids were purified, obtaining 101 CYP enzymes inside each capsid with a CYP internal occupation around 30%, and k_{cat} as 1198 min^{-1}. These capsids were subsequently functionalized with glucose oxidase using three different crosslinking reactions in order to evaluate the optimum conditions for efficient functionalization and obtaining maximum cascade reaction of GOx-CYP. Carbodiimide coupling was used to functionalize glucose oxidase as well as indocyanine green. The catalytic rate constant for P22-CYP-GOx nanoreactors with combined activity of GOx-CYP was estimated as k_{cat} = 187 min^{-1}. Finally, the nanoreactors were functionalized with IcG in a 1:150 molar ratio, obtaining a concentration of 2.84 μg of IcG per mg of nanoreactors. After IcG functionalization, 54% of the original combined enzyme activity was retained. The photophysical properties were characterized to corroborate the successful functionalization of indocyanine green. The UV-Visible analysis showed the maximum absorption peak of IcG at λ = 780 nm only in IcG-functionalized nanoreactors. P22-CYP-GOx-IcG were able to generate ROS and increase the temperature up to 3.6°C after excitation with near infrared light (λ_{ex} = 808 nm, power = 0.5 W). The complete characterization of the nanoreactors revealed their possible use in quadruple combination therapy against breast cancer, including enzyme-prodrug, photodynamic, photothermal, and starvation therapies. Future work involves further experiments using tamoxifen to evaluate the transformation into its active metabolites, as well as cytotoxic cell assays under different environments to test their effectiveness for *in vitro* studies.

Abstract approved by:

_____

Dr. Kanchan Chauhan

Dedicated to my family,
for their unconditional love,
and everything I have learned from them.

Acknowledgments

I would like to express my deepest gratitude to my supervisor, Dr. Kanchan Chauhan, for all the support she gave me throughout the project. The achievement of the established goals would not have been possible without her help.

I appreciate the equipment and the material that the bionanotechnology department provided me to finish my experiments. Thanks to all the support of my friends and the members of the department. I would like to recognize the technical assistance of Dr. Katrin Quester during this project.

I am grateful to the National Autonomous University of Mexico (UNAM) for giving me a quality education. The realization of this thesis was fund by the project UNAM-DGAPA IA201620.

A special acknowledgment to my friends and family, they were always there when I needed them, and also when not, I love you.

Table of contents

Abstract ii
Dedication iii
Acknowledgments iv
List of figures viii
List of tables x

1. Introduction 1
1.1. Cancer 1
1.1.1. Breast cancer 1
1.1.2. Breast cancer treatment 3
1.2. Smart nanomaterials for cancer therapy 4
1.2.1. Stimuli responsive nanoplatforms 4
1.3. Crosslinking of proteins 5
1.3.1. Reaction with glutaraldehyde 5
1.3.2. Carbodiimide chemistry 6
1.3.3. UGI four-component reaction 7
1.4. Enzyme kinetics 8
1.4.1. Enzyme activity 9
1.4.2. Michaelis-Menten kinetics 10
1.5. Enzyme cascade reactions 12

2. Background 14
2.1. Therapeutic nanoreactors for cancer therapy 14
2.2. Virus-like particles (VLPs) 15
2.3. Bacteriophage P22 16
2.4. Enzyme-prodrug therapy 17
2.4.1. Tamoxifen 17
2.4.2. Cytochrome P450 18
2.4.3. CYP from *Bacillus Megaterium* 19
2.5. Starvation and oxidation therapy meditated by glucose oxidase 20
2.6. Photodynamic and photothermal therapies 21
2.6.1. Photodynamic therapy 21
2.6.2. Photothermal therapy 23
2.6.3. Indocyanine green 24

2.7. P22 nanoreactors 25

3. Justification, hypothesis, and objectives 28
3.1. Justification 28
3.2. Hypothesis 28
3.3. General objective 28
3.4. Specific objectives 28

4. Methods 30
4.1. Purification and characterization of P22-CYP capsids 30
4.1.1. Ultracentrifugation and fast protein liquid chromatography (FPLC) 30
4.1.2. Quantification of P22 viral capsids 31
4.1.3. Densitometric analysis on SDS-PAGE gel 31
4.1.4. Confinement molarity and percent occupancy 32
4.2. Multi-functionalization of the nanoreactors 32
4.2.1. Glucose oxidase functionalization 19
4.2.2. Indocyanine green functionalization 33
4.3. Enzyme activity of P22 nanoreactors 34
4.3.1. Enzyme activity of glucose oxidase 34
4.3.2. Enzyme activity of cytochrome P450 34
4.3.3. Cascade enzyme activity of CYP 35
4.4. Photophysical properties after IcG functionalization 35
4.4.1. Quantification of indocyanine green on the nanoreactors 35
4.4.2. Absorption and fluorescence of the nanoreactors 36
4.4.3. Fluorometric reactive oxygen species assay 36
4.4.4. Thermal properties 36
4.5. Size distribution and zeta potential of nanoreactors 37
4.5.1. TEM characterization 37
4.5.2. DLS size distribution and Z potential 37

5. Results 38
5.1. Purification and characterization of P22-CYP capsids 38
5.1.1. Purification of P22-CYP capsids 38
5.1.2. Quantification of protein in P22 viral capsids 39
5.1.3. Densitometric analysis of proteins on SDS-PAGE gel 39
5.1.4. Confinement molarity and percent occupancy 41
5.2. Photophysical properties of the nanoreactors 42
5.2.1. Absorbance and fluorescence of the nanoreactors 42
5.2.2. Indocyanine green quantification 44
5.2.3. ROS generation assay 44
5.2.4. Temperature change of nanoreactors 46

5.3. Psychochemical properties of the nanoreactors 47
5.3.1. Size distribution and zeta potential – DLS 47
5.3.2. TEM characterization 48
5.4. Enzyme activity of the nanoreactors 50
5.4.1. CYP enzyme kinetics of P22-CYP capsids 50
5.4.2. Enzyme activity after each reaction for GOx functionalization 51
5.4.3. GOx-CYP combined enzyme kinetics of UGI 50 and EDC-NHS nanoreactors 55
5.4.4. Combined enzyme kinetics of the nanoreactors after IcG functionalization 56

6. Discussions 59
6.1. Enzyme-prodrug and starvation therapies 59
6.2. Photodynamic and photothermal therapies 62
6.3. Combination therapy 64

7. Conclusions 66

8. Perspectives 68

9. Appendix I. Tamoxifen functionalization approach 69

10. Bibliography 71

List of figures

Figure 1. Schematic representation of the glandular tissues in the breast 2
Figure 2. Mechanisms of protein crosslinking with glutaraldehyde under basic conditions 6
Figure 3. Schematic representation of the carbodiimide chemistry to conjugate two different proteins 7
Figure 4. Accepted reaction mechanisms of the four-component reaction proposed by Ugi in 1959 8
Figure 5. Product accumulation over a certain period in an enzyme reaction 9
Figure 6. Enzyme kinetics curve corresponding to the Michaelis-Menten model 10
Figure 7. Representation of the enzyme cascade of three enzymes (CelB, GALK, and GLUK) 13
Figure 8. Possible morphologies of P22. Procapsid (PC) is auto assembled in the presence of coat and scaffold protein 17
Figure 9. Structure of tamoxifen and some of its active metabolites 18
Figure 10. Glucose oxidase catalyzed reaction 20
Figure 11. Representation of the physical processes of a photosensitizer under light irradiation 22
Figure 12. Absorption spectra of different compounds found in tissues 23
Figure 13. Depth penetration of different wavelengths in the tissue 23
Figure 14. Representation of the P22 capsids with glucose oxidase and CYP used to transform endocrine disruptor compounds 26
Figure 15. Schematic representation of the enzyme-prodrug and photodynamic therapy proposed by Chauhan et al. 27
Figure 16. Elution profile of the P22 viral capsids with CYP activity obtained by size exclusion chromatography 38

Figure 17. SDS-PAGE gel with P22 viral capsids samples 40
Figure 18. Absorption spectra of the nanoreactors 42
Figure 19. Near-infrared fluorescence in different samples with PBS buffer, P22-CYP-GOx and P22-CYP-GOx-IcG nanoreactors, and IcG diluted in PBS 43
Figure 20. Calibration curve of indocyanine green to calculate the concentration in the nanoreactors 44
Figure 21. Fluorometric ROS production assay of the nanoreactors monitoring the conversion of DPBF 45
Figure 22. (Red) Cumulative change in temperature of P22-CYP-GOx-IcG nanoreactors under near-infrared light. (Blue) Cumulative change in the temperature of control with PBS buffer under near-infrared light 46
Figure 23. Size distribution for intensity of the functionalized nanoreactors 48
Figure 24. TEM micrographs of P22-CYP-GOx nanoreactors at different magnifications 49
Figure 25. Size distribution of the nanoreactors by TEM analysis 50
Figure 26. CYP enzyme kinetics of the P22-CYP nanoreactors 51
Figure 27. Combined enzyme activity of the nanoreactors after the functionalization of GOx with different reactions 54
Figure 28. Transformation kinetics of DMP by the glucose-mediated cascade reaction using UGI 50 and EDC-NHS nanoreactors 55
Figure 29. Transformation kinetics of DMP by glucose mediated cascade reaction using nanoreactors before and after IcG functionalization 57
Figure 30. Schematic representation of the processes that take place in the P22-CYP-GOx-IcG nanoreactors to achieve a combination therapy 64
Figure 31. Schematic representation of the different steps to obtain pegylated nanoreactors functionalized with a tamoxifen derivate using disulfide bonds 69
Figure 32. High resolution mass spectroscopy of TAM-OH 70

List of tables

Table I. Molecular subtypes of breast cancer and their hormone receptors expression 3
Table II. Reported therapeutic cancer nanoreactors 14
Table III. Cytochrome P450 enzyme activity obtained in different FPLC fractions 39
Table IV. Densitometric analysis to calculate CP and CYP-SP ratio 40
Table V. Zeta potential after each functionalization step 48
Table VI. Kinetic constants of the CYP in P22-CYP nanoreactors 51
Table VII. Glucose oxidase activity after each reaction of GOx functionalization 52
Table VIII. Cytochrome P450 specific activity after each reaction of GOx functionalization 53
Table IX. Specific activity of CYP by glucose mediated cascade reaction 54
Table X. Enzyme kinetic constants for DMP transformation by UGI 50 and EDC-NHS nanoreactors 55
Table XI. Catalytic constants for DMP transformation using the nanoreactors after each functionalization step 57

1. Introduction

1.1. Cancer

Cancer is a health problem worldwide; it is estimated that more than eight million people will die for this disease in 2020, this is about the entire population of Switzerland. Every year the number of new cases is growing at an alarming rate in all the countries no matter their economic, cultural, or social situation [1]. The economic impact of cancer is another important element to consider; in 2008, the economic loss associated with cancer consequences was estimated at 895 billion dollars. Lung, colon, and breast were the cancers with the highest economic impact reported [2].

Cancer is caused by a combination of various factors. The main lifestyle factors linked to this disease are sedentary lifestyle, obesity, smoking, alcoholism, unhealthy diet, among others; these factors are more common in the highly globalized world [3]. On the other hand, cancer is inherently a genetic disease that undergoes an accumulation of random mutations at more than one gene. Usually, long periods are required for these cell mutations to start being a health complication [4].

1.1.1. Breast cancer

Currently, breast cancer is the leading cause of mortality in women around the world. In 2017, approximately 600,000 women died due to this disease [5]. Breast cancer represented 24% of the new cancer cases on women and 15% of the deaths in 2018. Different studies have correlated the role of genes BRCA1, BRCA2, and hereditary factors with breast cancer susceptibility. Nevertheless, the most important factors as in different types of cancers, are environmental ones [6]. The various non-genetic risk for breast cancer includes birth control

methods, not breastfeeding or not having children, alcoholism, chest radiation exposure, and hormone replacement therapy after menopause [7].

Breast cancer is defined as the uncontrolled growth and proliferation of cells in the breast tissue. Breast is composed of various tissues; two of them are the milk-producing glands that are grouped in lobules, and the ducts that serve to transport the milk (Figure 1). Ductal and lobular breast cancers are the most common among women; however, cancer can start in other tissues such as the fatty connective tissue [8]. Depending on the type of cells, cancer can be grouped in carcinomas and sarcomas; carcinomas have a begin from epithelial cells, while sarcomas derivate from stromal components [7].

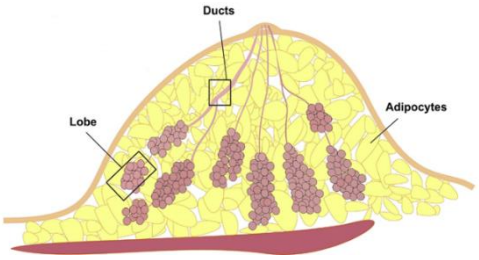

Figure 1. Schematic representation of the glandular tissues in the breast. Lobular and duct cells are more likely to transform into cancer cells. Modified from Zeng et al., 2020 [75].

According to the dissemination, breast cancer can be cataloged in an invasive or non-invasive type. Invasive cancers are those that are disseminated in various tissues, while non-invasive are found in one specific tissue. Lobular carcinoma *in situ* and ductal carcinoma *in situ* are the two most common types of breast cancer; these types also includes their invasive variants, infiltrating lobular carcinoma and infiltrating ductal carcinoma [8].

Breast cancer can be classified in their molecular subtypes on the basis of the over or the non-expression of different hormone receptors. Luminal A, luminal B, HER2-enriched, triple-negative, and normal-like breast cancers are six molecular subtypes characterized by

an abnormal expression of estrogen receptors (ER), progesterone receptors (PR), and human epidermal growth factor receptor 2 (HER2) (Table I) [7].

Table I. Molecular subtypes of breast cancer and their hormone receptors expression. Modified from Feng et al., 2018 [7].

Subtypes	**Molecular signatures**	**Characteristics**
Luminal A	ER+, PR±, HER2-	Most common & best prognosis
Luminal B	ER+, PR±, HER2±	Lower survival than luminal A
HER2	ER-, PR-, HER2+	5-15% of breast cancers
Triple-negative	ER-, PR-, HER2-	Worst prognosis
Normal-like	ER+, PR±, HER2-	Rare

Luminal breast cancer is characterized by the expression of ER and PR; therefore, it can be treated blocking these receptors and thus limiting cell growth. HER2-enriched breast cancer does not express ER or PR, but some medications, such as Herceptin, are targeted to the protein HER2 to reduce cancer cell proliferation. Triple-negative cancer does not have the expression of any hormone receptors and thus, it is the most aggressive type of breast cancer. Recently, novel treatment strategies have been proposed to fight against this subtype [8].

1.1.2. Breast cancer treatment

Tumor size and stage, the subtype of breast cancer, the presence of mutations (i.e. BRC1 or BRC2 genes), and patient's health are the common factors that are considered in the selection of optimal treatment. The most prevalent therapies used in breast cancer are surgery, chemotherapy, radiotherapy, hormonal therapy, targeted therapy, and immunotherapy [8].

Three different molecular targets have been identified in most breast cancers, ER is present in almost 70% of invasive cancers and HER2 is overexpressed in 20% of them. These receptors have been extensively studied to design hormone therapies against breast cancer.

For non-metastatic cancers, surgery is usually the first option to remove the tumor, followed by radiation and hormone therapies to prevent relapse. Metastatic breast cancer has high mortality rates and most of the cases are incurable; in this situation, surgery and radiation can prolong the patient's life [9].

1.2. Smart nanomaterials for cancer therapy

Conventional cancer therapies have undesirable side effects, some of them are related to the lack of selectivity of the agents used (i.e. chemotherapy drugs, radiation sources). This non-selectivity can lead to either damage of adjacent tissues in the case of radiotherapy, or systemic damage in the case of chemotherapy [8,124].

With the recent development of nanotechnology, new methods for the diagnosis, *in vivo* imaging, detection of biomarkers, and the design of novel cancer therapies have been reported [124]. The use of nanocarriers for the delivery of compounds -such as antibodies, peptides, fluorescent markers, and others- into cancer cells, increase the selectivity and diminish the side effects of the conventional therapies, furthermore, have opened a new gate for the design of more efficient cancer therapies [123].

Smart nanomaterials are characterized by an enhanced selectivity mediated by the use of target receptors for ligand molecules and other techniques such as the highly localized irradiation of light in the presence of photosensitizers and photothermal absorbers [125].

1.2.1. Stimuli responsive nanoplatforms

High glucose levels in cancer cells promote proliferation and increase the probability of dissemination. In order to grow, tumors need a microenvironment (TME) with a high concentration of glucose [126,127]. For this reason, glucose-responsive nanoplatforms have been used in novel cancer therapies. One approach consists of the delivery of glucose

oxidase, which catalyzes the transformation of glucose into gluconic acid, diminishing glucose concentration in the TME, and decreasing tumor growth [32,33]. Light responsive nanoplatforms for *in vivo* imaging of tumors or the use of photodynamic or photothermal therapies have also been reported [42,43,117].

1.3. Crosslinking of proteins

Crosslinking is a process that involves the formation of covalent bonds between two or more molecules. In the case of proteins, crosslinking usually consists of the use of reagents that react with functional groups of the amino acid residues and facilitate the formation of covalent bonds between proteins. The crosslinker agents can be either homo or hetero-bifunctional depending if their reactive groups on both sides of the molecule are identical or not [78].

1.3.1. Reaction with glutaraldehyde

One commonly used reagent for the crosslinking of proteins is glutaraldehyde. It is a homobifunctional reagent that reacts with amino groups to generate stable crosslinking. Due to the different forms that glutaraldehyde can adopt in aqueous solutions -including its polymerization, the formation of dimeric cyclic glutaraldehyde, among other forms-, the mechanism to crosslink proteins is not well understood. However, several mechanisms have been proposed and depend on the pH and the presence of different functional groups.

At neutral or basic pH glutaraldehyde forms polymeric structures. Two mechanisms are generally accepted to stabilize the protein crosslinking in these conditions, one implies the formation of Schiff bases that are stabilized by resonance with double bonds, and the other a Michael-type addition (Figure 2) [53].

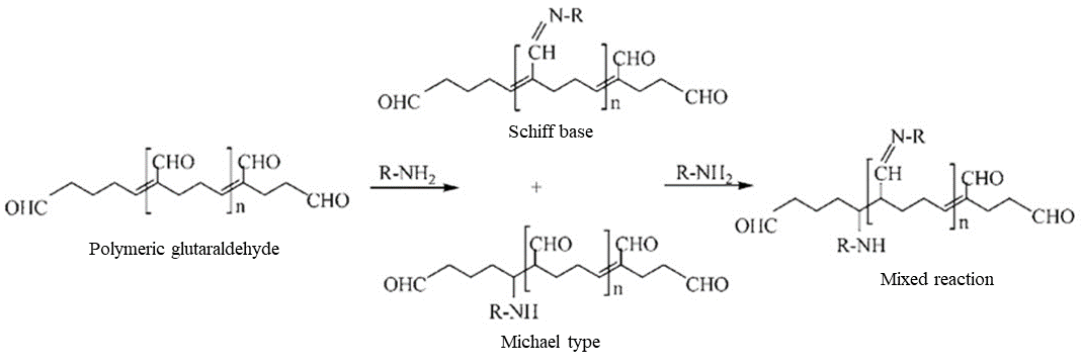

Figure 2. Mechanisms of protein crosslinking with glutaraldehyde under basic conditions. The formation of Schiff bases and Michael-type additions are the most accepted mechanisms. Modified from Migneault et al., 2004 [53].

Proteins contain lysine residues that are mostly exposed on the surface and most of them do not play a role in the catalytic site, this characteristic permits the crosslinking of enzymes using glutaraldehyde preserving the conformation and catalytic activity [79,80].

1.3.2. Carbodiimide chemistry

1-Ethyl-3-(3-dimethylaminopropyl)carbodiimide or EDC is a zero-length crosslinker that leads to the conjugation of carboxylates and primary amines, forming amide covalent bonds between the desired molecules. In the case of proteins, the carboxylic acids in amino acid residues can react with EDC to form an o-acylisourea intermediate that is easily displaced by a nucleophilic attack from primary amino residues of other proteins [81].

N-hydroxysuccinimide or NHS is usually used in carbodiimide chemistry due to the high stability that NHS-ester intermediates have in dry conditions. NHS prevents the easy hydrolysis of the o-acylisourea intermediate and improves the efficiency of the conjugation (Figure 3) [81].

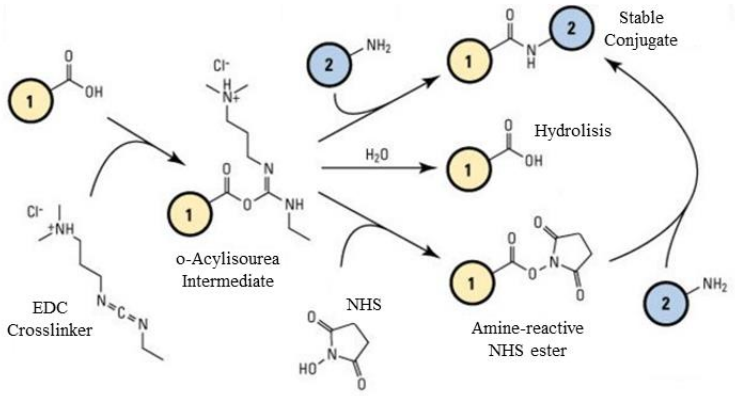

Figure 3. Schematic representation of the carbodiimide chemistry to conjugate two different proteins. EDC reacts with a carboxylic acid to form an intermediate; subsequently, NHS can react with this intermediate to form a more stable NHS-ester that reacts with a primary amine to form an amide bond to conjugate the proteins. Modified from Thermo Scientific [82].

One advantage of this method of crosslinking is that EDC, NHS, and the isourea byproduct formed in this reaction are water-soluble and can be removed by dialysis or gel filtration. For the crosslinking of proteins with this procedure, the optimal range of pH is from 4.5 to 7.5, beyond these values, the reaction is slower, and with a lower yield [81].

1.3.3. UGI four-component reaction

The four-component reaction was proposed by Ivar Ugi in 1959 [48], it involves the use of an aldehyde, an amine, a carboxylic acid, and an isocyanide to form the final α-acetoamido carboxamide derivate.

Two principal mechanisms are accepted, in the first step of both the aldehyde reacts with the amine to form an imine, from this point the two mechanisms undergo different intermediates until the formation of an imidate, which is subsequently transformed into the final derivate by the Mumm rearrangement (Figure 4) [83].

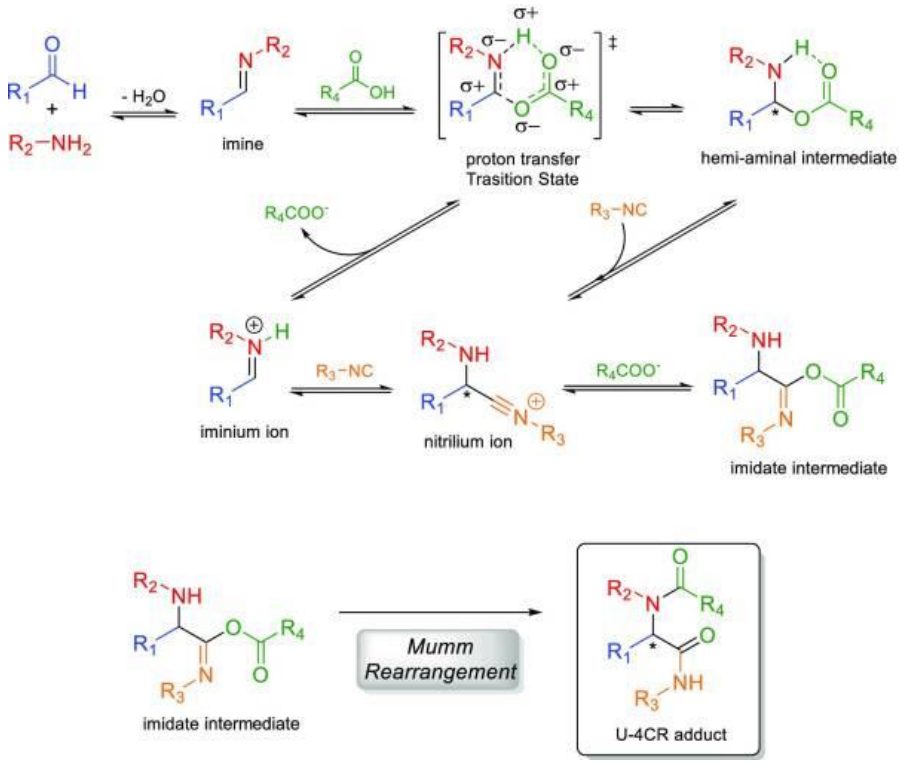

Figure 4. Accepted reaction mechanisms of the four-component reaction proposed by Ugi in 1959 [48]. It consists of the use of an amine, an aldehyde, a carboxylic acid, and an isocyanide to form an α-acetoamido carboxamide derivate. Modified from Rocha et al., 2020 [83].

Different bioconjugation reactions -such as lipid-lipid, peptide-peptide, peptide-steroid, enzyme immobilization in protein carriers, among others- have been reported using the Ugi four-component reaction. These approaches take advantage of the functional groups of the lipids, carbohydrates, and proteins to conjugate these molecules by the mechanisms of the Ugi reaction [84-87].

1.4. Enzyme kinetics

Enzymes are biological catalysts made of proteins that lower the energy of activation (E_a) of a reaction, increasing the transformation rate without affecting the reaction equilibria. An enzyme decreases the E_a binding to and stabilizing the transition state of the reaction. Unlike other types of catalysts, enzymes are highly specific, and they usually catalyze a single reaction [90].

1.4.1. Enzyme activity

Progress curves monitoring the generation of products over certain periods have been used to determine the reaction velocity. This velocity corresponds to the slope of the curve at specific time. Several factors decrease the reaction velocity, some of these are the decrement in the saturation of the enzyme, the induced reverse reaction by the accumulation of product, and the inhibition of the enzyme by the products. To reject the influence of these factors, the initial velocity is usually calculated. These measurements are generally performed with various substrate concentrations until the saturation of the enzyme (Figure 5) [90].

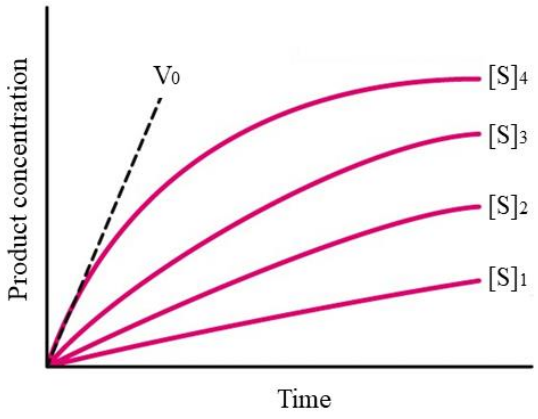

Figure 5. Product accumulation over a certain period in an enzyme reaction. The initial rate of the product generation is usually used to calculate the reaction velocity. Modified from Berg et al., 2012 [91].

To simplify the measurement of the reaction velocity of enzymes, the enzyme unit (U) is generally used, it is defined as the amount of enzyme that catalyzes the transformation of 1 µmol of substrate per minute. The specific activity is defined as the number of enzyme units per mass (U/mg), where the mass can correspond to the enzyme, the total protein in the solution, etc. Another concept used in enzymology is the turnover number (k_{cat}), which corresponds to the number of substrate molecules transformed to product per molecule of enzyme per unit of time (usually expressed as s^{-1} or min^{-1}) [90].

1.4.2. Michaelis-Menten kinetics

The Michaelis-Menten kinetics is a model that describes the behavior of some enzymes considering the steady state. It relates the concentration of the substrate with the reaction velocity using two kinetic parameters, K_M and V_{max}. The Michaelis-Menten constant K_M represents the substrate concentration at half of the maximum velocity, K_M relates all the rate constants as described later. On the other hand, the maximum velocity (V_{max}) represents the rate of product transformation when all the enzyme is in the form of the enzyme-substrate complex. To determine the K_M and V_{max}, the initial enzyme activity is measured at different substrate concentrations. If the enzyme kinetics can be described with this rectangular hyperbolic model, a Michaelis-Menten curve is adjusted (Figure 6) [92].

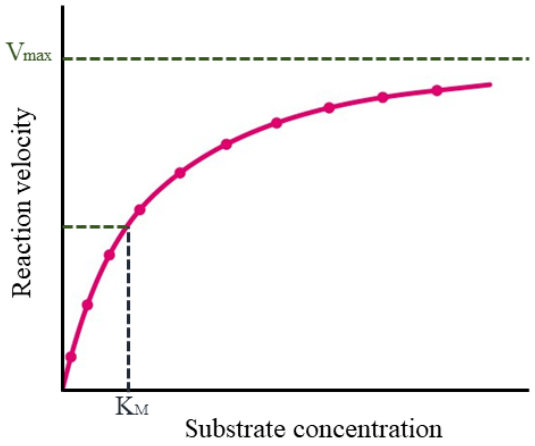

Figure 6. Enzyme kinetics curve corresponding to the Michaelis-Menten model. K_M represents the substrate concentration necessary to reach half of the maximum velocity (V_{max}). Modified from Berg et al., 2012 [91].

In this model, the substrate (S) binds reversibly to the enzyme (E) to form an intermediate enzyme-substrate (ES) complex, that finally will be irreversible transformed to the product (P) and the free enzyme (E) (Equation 1) [92].

$$E + S \underset{k_{-1}}{\overset{k_1}{\rightleftharpoons}} ES \xrightarrow{k_2} E + P \qquad \text{[Eq. 1]}$$

The equation of the time-dependent change in the ES complex can be rewritten considering its formation and consumption (Equation 2).

$$\frac{d[ES]}{dt} = k_1[E][S] - k_{-1}[ES] - k_2[ES] \quad \text{[Eq. 2]}$$

The equation can be rearranged considering that the reaction is at the steady state, thus the change in the concentration of the ES complex over time is zero (Equation 3).

$$k_1[E][S] = (k_{-1} + k_2)[ES] \quad \text{[Eq. 3]}$$

The total enzyme concentration E_T is equal to the sum of the free enzyme E and the enzyme in the ES complex, considering this, the equation can be rewritten (Equation 4).

$$([E_T] - [ES])[S] = \left(\frac{k_{-1}+k_2}{k_1}\right)[ES] \quad \text{[Eq. 4]}$$

Michaelis-Menten constant K_M is defined as follows (Equation 5):

$$K_M = \left(\frac{k_{-1}+k_2}{k_1}\right) \quad \text{[Eq. 5]}$$

The rate of product formation *v* is defined as the rate constant k_2 multiplied by the concentration of the ES complex, thus $v = k_2[ES]$. Substitution of Eq. 5 in Eq. 6 and further expression in terms of *v* lead to a new equation (Equation 6).

$$[E][S] = \frac{v}{k_2}(K_M + [S]) \quad \text{[Eq. 6]}$$

The maximum rate of product formation V_{max} of the reaction takes place when all the enzyme is in the form of the enzyme-substrate complex, thus [E] = [ES]. Considering $v = k_2[ES]$, it can be obtained the expression $V_{max} = k_2[E]$, and it can be substituted in Eq. 6 (Equation 7).

$$v = \frac{V_{\max}[S]}{K_M + [S]} \quad \text{[Eq. 7]}$$

Michaelis-Menten equation (Eq. 7) describes the behavior of this respective model. Two parameters are characteristic in this equation, an asymptote in $v = V_{max}$ and a characteristic substrate concentration K_M at $v = 0.5*V_{max.}$

1.5. Enzyme cascade reactions

Enzyme cascade reactions are observed in multiple cell metabolic pathways, they usually involve the use of various enzymes, and the product of every single reaction may be used as reagent for other reactions, creating complex pathways. Enzyme cascades have an endpoint characterized for the release of the desired product outside the active-site microenvironment [128,129].

Multienzyme immobilization is an effective method to mimic cascade reaction pathways, some of its advantages are the use of smaller reactor volumes, shorter time cycles, and less waste generation. Furthermore, higher stability in immobilized enzymes plays also an important role. Co-immobilization of enzymes in nanocarriers using random strategy, positional strategy, and compartmentalization has been extensively studied [129,130].

Multienzyme cascade reactions within viral capsids were reported by Patterson et al. in 2013, they fused three enzymes (GALK, GLUK, and CelB) to the scaffold protein of the P22 and expressed it with the coat protein; their nanoreactors showed the activity corresponding to the cascade system using lactose and ATP as substrates in citrate buffer (Figure 7). [104]. Recently, González-Davis et al, reported a two-enzyme cascade system in P22 viral capsids to transform endocrine disruptor compounds solely in the presence of glucose, they used glucose oxidase functionalized to the surface of the P22 and cytochrome P450 fused to the scaffold protein [45].

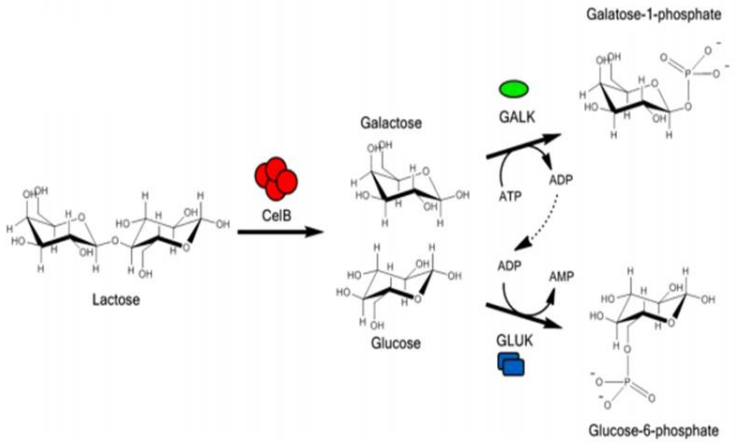

Figure 7. Representation of the enzyme cascade of three enzymes (CelB, GALK, and GLUK). Lactose and ATP are used as the substrates to generate glucose-6-phosphate ad galactose-1-phosphate. Modified from Patterson et al., 2013 [104].

2. Background

2.1. Therapeutic nanoreactors for cancer

Nanoreactors are nanometric confined spaces in which a catalytic reaction takes place. Usually, the nanoreactors contain catalysts such as inorganic catalysts, enzymes, proteins, and synthetic compounds that undergo catalytic transformations. Their study for biomedical applications has notably increased due to the advantages of these systems versus the conventional ones. These advantages include the protection of the catalysts against harsh environments (i.e. extreme pH), enhanced protease resistance, higher catalytic efficiencies of the enzymes due to the confined spaces, among others [10].

Several therapeutic nanoreactors have been reported in the last years (Table II). These have shown high efficiency in the transformation of prodrugs into active drugs, increasing the effectiveness and reducing the side effects of cancer therapy, which is called enzyme-prodrug therapy [11]. Other nanoreactor systems use simultaneous reactions to achieve an enhanced photodynamic therapy (PDT), increasing the production of reactive oxygen species (ROS) while decreasing the concentration of glucose and O_2 in cancer cells [12].

Table II. Reported therapeutic nanoreactors. Modified from Mukerabigwi et al., 2018 [10].

Nanovehicle	Function	Delivery compound	Reference
Polymersomes	ROS generation to enhance PDT therapy	Rose Bengal, bovine serum albumin (BSA)	Baumann et al., 2014 [13]
Inorganic nanoparticles	Tumor starvation, H_2O_2 generation	Glucose oxidase, Fe_3O_4 NP's	Huo et al., 2017 [14]
Micelles	Enzyme-prodrug therapy	Palladium NP's, doxorubicin	Miller et al., 2017 [15]
Virus-like particles	Enzyme therapy	GALT enzyme	Gama, P., 2019 [16]

Some nanoreactors carry enzymes and other biological compounds that perform a reaction in a specific target. Various types of nanocarriers have been reported: liposomes, polymersomes, inorganic nanoparticles, micelles, and virus-like particles (VLPs) are some examples of compound transporters used for cancer treatments [10].

According to LeDuc et al. [93], five requirements are necessary for nanoreactors: the presence of a structural compartment, good permeability, accumulation in the target site, encapsulation of the desired compounds, and self-destruction. Some important factors to consider in the design of nanoreactors are the high encapsulation of the enzymes without a great loss in the activity, a good purification of the nanoreactors -as this can cause immune responses-, and the stability of nanoreactors in physiological environments to prevent a release of the delivered compounds before reaching the target site [94].

Long-term blood circulation plays a key role in the therapeutic use of the nanoreactors, this characteristic can be enhanced by functionalizing biocompatible polymers such as PEG and poly-amino acids, this functionalization reduces the proteolysis or the elimination of the nanoreactors by the mononuclear phagocytic system [94].

2.2. Virus-like particles (VLPs)

Viruses are infectious microorganisms composed of nucleic acids and proteins, and they proliferate by injecting their genetic material i.e. nucleic acids in the host cell. Without nucleic acids, the virus is just a protein shell capable of encapsulating and be functionalized with different bioligands. This characteristic can be used for the delivery of selected drugs and biomolecules to cancer cells. Currently, the use of viral capsids for drug delivery into cancer cells and other diseases is extensively studied [17].

Virus-like particles are viral capsids that lack genetic information and thus they are not infectious. They are constructed by the self-assembly of hundreds to thousands of proteins to form complex structures. Some advantages of these structures are the inherent biocompatibility, the relative ease of functionalization, and morphological uniformity [18].

Plant viruses and bacteriophages are potential VLPs due to the lack of toxicity in humans. The cowpea chlorotic mottle virus (CCMV) capsids have icosahedral symmetry with an average diameter of 28 nm, the N-residues on the surface of these capsids are suitable for the covalent union of other molecules. Another plant viruses such as brome mosaic virus (BMV) and cucumber mosaic virus (CMV) have been studied for the encapsidation of various compounds. The use of virus-like particles from bacteriophages has been successfully reported, and the most commonly used are MS2 and P22 [19].

2.3. Bacteriophage P22

Viral capsids of *Salmonella typhimurium* bacteriophage P22 need 420 copies of coat protein (CP) produced by gene 5 that are assembled with 100-300 copies of scaffold protein (SP) produced by gene 8. The molecular weight of CP and SP is 46.6 and 33.6 kDa respectively. Self-assembly of P22 capsid in the presence of these proteins is one of the most important characteristics of this system, P22 procapsid adopts a T=7 icosahedral structure with an external diameter of 58 nm. After thermal treatment, procapsids change their morphology [21].

Expanded shell structure is formed after 10 minutes at 65°C, the average diameter of this expanded shell is 64 nm; while wiffleball morphology is obtained after 20 minutes at 75°C, it has 10 nm holes at each of the 5-fold vertices (Figure 8) [20]. Procapsid shell structure is composed of 71 capsomers, 60 of them hexameric and 11 pentameric oligomers [21].

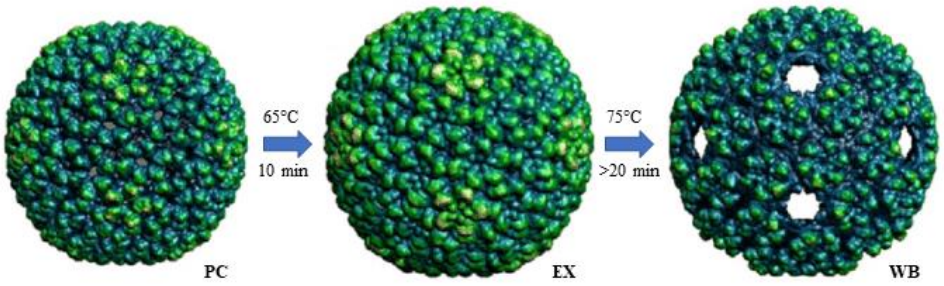

Figure 8. Possible morphologies of P22. Procapsid (PC) is auto assembled in the presence of coat and scaffold protein. Expanded shell (EX) and wiffleball (WB) are obtained after a thermal treatment. Modified from Wu et al., 2013 [22].

In 2012, Patterson et al. reported the encapsidation of beta-glucosidase (CelB) into P22 capsids, in this study the scaffold protein was fused with CelB and co-expressed with the coat protein to achieve P22 nanoreactors with a high concentration of CelB enzyme encapsidated, and with no loss in the activity [103]. In 2013, the same group reported the co-encapsidation of two and three enzymes inside P22 capsids to achieve a cascade reaction [104]. Various biomedical applications of P22 viral capsids are described in section 2.7. of this thesis.

2.4. Enzyme-prodrug therapy

Some disadvantages of chemotherapy are the dramatic side effects that lead to systemic damages to the organs, insufficient drug concentration at cancer cells, the resistance of some drugs, and the non-selectivity in most of the commonly used drugs. Enzyme-prodrug therapy involves the controlled expression of a drug-activating enzyme in the cancer tumors and the subsequent delivery of a prodrug. These enzymes transform the prodrug into its active form, diminishing side effects, and increasing the drug concentration in cancer cells [23].

2.4.1. Tamoxifen

Tamoxifen is the most used anti-estrogen prodrug to treat ER+ breast cancers. It is usually prescribed as an adjuvant drug after surgery for a period of 5 years, or in women with a high risk of developing breast cancer. Some studies have reported a reduction in recurrence and

mortality using tamoxifen in early cancer stages [24]. This prodrug is metabolized by the cytochrome P450 enzymes, the active metabolites of tamoxifen are N-desmethyl-tamoxifen, 4-hydroxy-tamoxifen, and N-desmethyl-4-hydroxytamoxifen (Figure 9) [25].

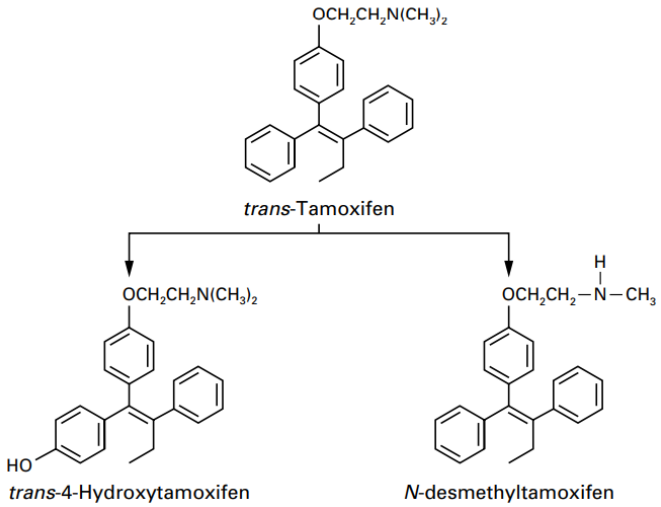

Figure 9. Structure of tamoxifen and its important active metabolites. Tamoxifen is transformed into *trans*-4-Hydrotamoxifen and N-desmethyltamoxifen by the catalytic action of cytochrome P450 enzymes. Obtained from Osborn et al., 1998 [25].

The mechanism of action is based on its ability to compete with estrogen and bind to estrogen receptors. As a result, it inhibits the expression of estrogen-regulated genes and prevents cancer cell proliferation. However, high mutagenic potential and cellular resistance after a prolonged use of drug have been reported. Nevertheless, the advantages of the tamoxifen against breast cancer cells justify its extensive use in breast cancer treatment [25,26].

2.4.2. Cytochrome P450

Cytochrome P450 (CYP) is a superfamily of hemoproteins named after its characteristic absorbance peak at 450 nm. Depending on the type of organism, these proteins have different functions. CYP present in prokaryotic organisms can be useful in the biosynthesis of antibiotics and the bioremediation of polluting compounds. In plants, CYP is important for the synthesis of phytohormones and other compounds. Human CYP is well known for its

role in phase I of the drug metabolism, the main goal of this phase is to introduce or expose functional groups with the oxidation, reduction or hydrolysis of the original molecule.

In the case of cancer drugs - such as tegafur, docetaxel, cyclophosphamide, tamoxifen, among others-, CYP modulates the reactions to generate the active compounds [27,105]. Of this superfamily, CYPs 2C9, 2D6, and 3A4 are responsible for the majority human drug oxidations [106].

In the specific case of tamoxifen, the CYP3A subfamily is responsible for its transformation into N-desmethyl-tamoxifen, a metabolite less active than tamoxifen. The two other metabolites, 4-hydroxytamoxifen, and endoxifen have 100 times more affinity as estrogen antagonists than tamoxifen and are mainly generated by CYP2D6 [105].

Genetic and environmental factors are known to alter the activity of CYP2D6, thus affecting the effectiveness of tamoxifen [107]. Moreover, CYP enzymes are down-regulated in breast cancer tumors; CYP1B1 is usually found in breast cancer tissues, while CYP3A shows negligible expression in breast cancer tumors [108-110]. Recently, a novel approach to reach an enhanced enzyme-prodrug therapy was developed, it consists of the controlled delivery or expression of specific CYP enzymes in cancer cells [111].

2.4.3. CYP from *Bacillus megaterium*

The variant CYP_{BM3} obtained from *Bacillus megaterium* has higher solubility and stability compared with other types of CYP. For this reason, several induced mutations have been reported to increase its catalytic activity for various substrates. One of these variants, CYP_{BM3}21B3 was generated by Cirino and Arnold in 2003, it consists of the heme domain. and contains the mutation F87A, nine amino acid substitutions, from which 4 mutations are placed in the protein surface. This specific variant exhibits an improved peroxidase activity

for the use of H_2O_2 as the final electron acceptor; in this way, NADPH and the reductase domain are no longer needed [28,29].

This variant of the CYP has been used for different applications. In 2011, Sánchez-Sánchez et al. reported the use of this enzyme to transform organochlorine and organophosphorus compounds into its derivates that are more susceptible to biological degradation and have less toxicity; this showed the potential use of $CYP_{BM3}21B3$ for environmental purposes [29]. In another study, this variant of the CYP was used to transform resveratrol to piceatannol without the use of the expensive cofactor NADPH, showing a maximum activity in pH 8.5-9 and 80°C [102]. Other biomedical applications of $CYP_{BM3}21B3$ are discussed in section 2.7. of the present thesis.

2.5. Starvation and oxidation therapy mediated by glucose oxidase

Starvation therapy is a new method to decrease the concentration of glucose and oxygen in cancer cells while increasing cytotoxic hydrogen peroxide. This therapy uses the enzyme glucose oxidase (GOx) that catalyzes the oxidation of glucose into gluconic acid and H_2O_2 (Figure 10) [30].

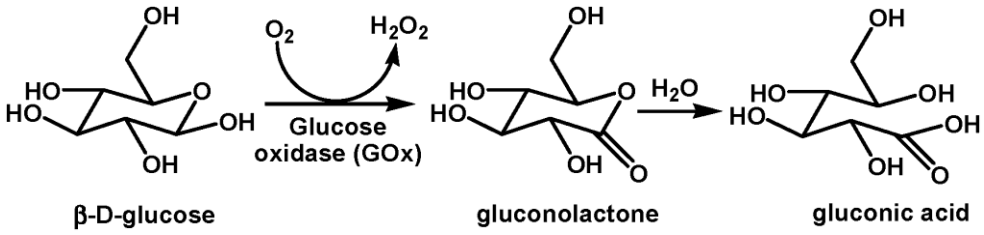

Figure 10. Glucose oxidase catalyzed reaction. The transformation of glucose into gluconic acid is catalyzed by glucose oxidase. Obtained from Dinda et. al., 2018 [31].

After targeted delivery of glucose oxidase into tumor cells, different processes take place. A decrease in the concentration of glucose, the main source of energy, leads to starvation therapy; at the same time, a reduction in O_2 levels activates hypoxia. On the other hand, an

increase in the concentration of hydrogen peroxide and gluconic acid start a process of oxidation and allow pH-responsive drug release [32].

Liposomes, nanogels, and other nanovehicles have been functionalized with glucose oxidase to reach oxidation, starvation, and hypoxia-activated therapies against cancer cells. In those studies, cell viability decreases with the use of glucose oxidase. Moreover, the systematic toxicity of GOx is dramatically reduced when it is transported by the nanocarriers to the cancer tumors [30,33].

2.6. Photodynamic and photothermal therapies

2.6.1. Photodynamic therapy

Photodynamic therapy (PDT) is a therapeutic approach that involves the use of a source of light to activate - in the presence of molecular oxygen- certain dyes called photosensitizers (PS) [95]. The advantages of PDT over conventional therapies are the lack of long-term side effects, as the newer PSs have a half-life of a few days and are often eliminated of the body within one week, the selectivity of the irradiated site and the possibility of multiple applications within short periods, the lower cost compared with other therapies, among others [76].

Photosensitizers are molecules that undergo photocatalytic reactions stimulated by the excitation of a specific wavelength of light. In PDT, after the controlled administration of photosensitizers in cancer cells, the tumor is irradiated with a specific wavelength of light to transform O_2 into singlet ($^1O_2$) and triplet oxygen ($^3O_2$), for the subsequent generation of reactive oxygen species (ROS) [34].

In the irradiation process, one electron of the PS molecule is excited to a higher energy orbital, to go back to the ground state the PS can emit this energy as fluorescence or heat. Another mechanism to release the energy is an intersystem crossing to form a triplet state, in this state the system can transfer energy to transform the triplet oxygen into singlet oxygen, these are called type II reactions. For the type I reactions, PS reacts with another molecule acquiring a hydrogen atom, or electron to form a radical (Figure 11) [35].

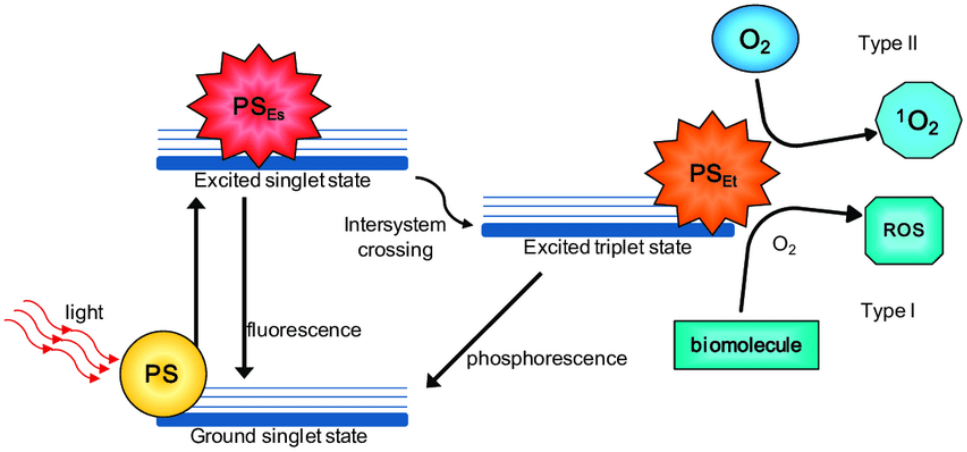

Figure 11. Representation of the physical processes of a photosensitizer under light irradiation. Obtained from Calixto et al., 2016 [76].

Some considerations related to the absorption wavelengths need to be taken when choosing the optimal photosensitizers. In order to generate $^1O_2$, the energy of the photons absorbed by the PSs needs to be enough to cause the excitation of the triplet state into the singlet oxygen. Some studies reported that above 850 nm, the efficiency in the generation of $^1O_2$ decreases significantly [96,97].

The interaction of light in the tissues has been extensively studied, the optical window is a region of the spectrum between 650 to 1200 nm with the maximum penetration depth in the tissues. This occurs because of scattering and autofluorescence decrease with higher wavelengths. Furthermore, some molecules -such as water, melanin, and hemoglobin (Hb)- have low absorption within the optical window (Figure 12) [98,101].

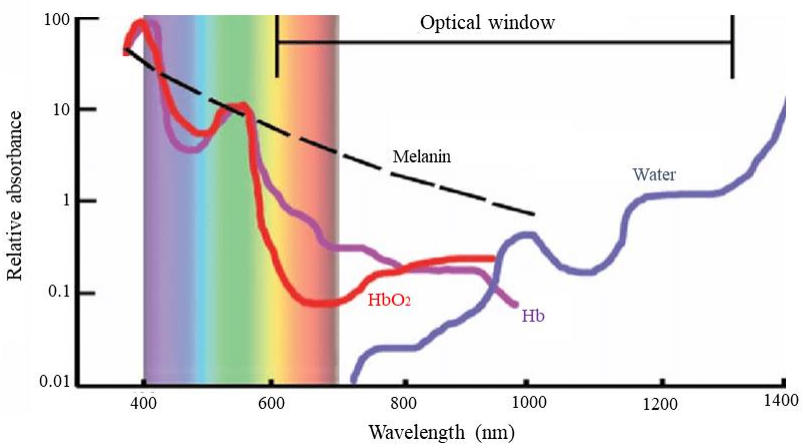

Figure 12. Absorption spectra of different compounds found in tissues. Due to the low absorbance of water, melanin, and hemoglobin (Hb) within the optical window (650-1200 nm), these wavelengths are preferred for maximum penetration of the light in the tissue. Modified from Lyons et al., 2013 [99].

Photons with wavelengths in the near-infrared (NIR) region of the spectrum show the deepest penetration in skin tissue, thus PSs with absorbance in this region are ideal if a high penetration is required (Figure 13) [100].

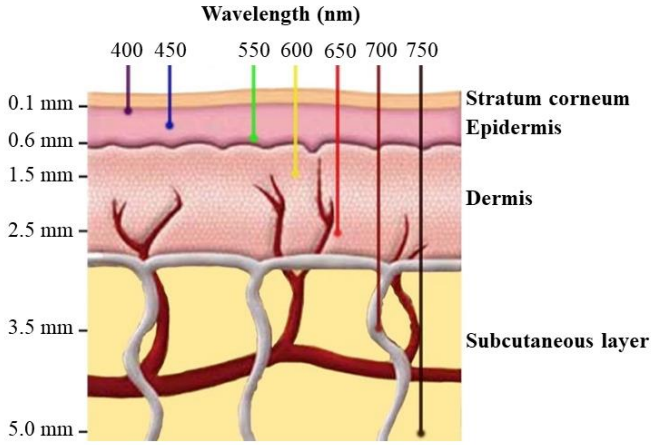

Figure 13. Depth penetration of different wavelengths in the tissue. NIR wavelengths are optimal for maximum penetration. Modified from Wang et al., 2015 [101].

2.6.2. Photothermal therapy

Photothermal therapy (PTT) consists of the use of near-infrared (NIR) light to illuminate topically or intestinally the cancer tumor, this light is transformed into heat, increasing the temperature of the cell, and causing protein denaturalization and damage to cell membranes. NIR light is used because of its deep penetration in the tissues [36,37]. To enhance PTT, NIR photothermal-absorber compounds are used; these can be classified in inorganic, carbon-based, and polymeric materials [112].

In hyperthermia therapy, cancer cells are heated above 41°C to start causing a decrease in the viability. Moderate increments in the temperature (40-43°C) can lead to a synergetic combination therapy when using cytotoxic drugs. Hyperthermia can induce apoptosis and membrane blebbing in cells below 43°C, and above that temperature necrosis has been reported. Moreover, between 42 to 45°C the intracellular de novo synthesis and polymerization of DNA and RNA in protein synthesis are decreased; furthermore, denaturalized proteins begin to aggregate at the nuclear matrix [113].

Some nanomaterials exhibit absorption in the NIR region of the spectrum, so their potential application in PTT has been studied [112]. Colloidal gold nanoparticles, gold nanorods, and other nano-morphologies of gold can absorb NIR light by surface plasmon resonance, but their application is limited due to toxicological concerns [114]. Graphene oxide and single-wall carbon nanotubes are effective photothermal absorbers and have been characterized for their application in PTT [115,116]. A more feasible approach is the use of fluorescent dyes -such as chlorine e6 or indocyanine green- functionalized in nanocarriers to achieve a PTT [117-119].

2.6.3. Indocyanine green

Sodium 4-[2-[(1E,3E,5E,7Z)-7-[1,1-dimethyl-3-(4-sulfonatobutyl)benzo[e]indol-2-ylidene] hepta-1,3,5-trienyl]-1,1-dimethylbenzo[e]indol-3-ium-3-yl]butane-1-sulfonate, best known

as indocyanine green or IcG, is a compound with photothermal, fluorescence, and photosensitizer properties [38]. IcG is a water-soluble dye approved by the FDA, it has low toxicity in the body and produces reactive oxygen species (ROS) under near-infrared irradiation [39].

The absorption and emission of IcG are in the near-infrared region of the spectrum, with a maximum value at 780 and 830 nm respectively. The fluorescence output of IcG is high even in small concentrations [40,41]. This absorption lies in the optical window, and NIR light is known for deep penetration into the tissue, therefore, IcG can be used in photodynamic therapy against cancer in tumors with maximum depth about 5 mm [100].

Several studies have successfully reported the synthesis and optimization of IcG-functionalized nanoplatforms for their use to reach a combined chemo-photothermal and photodynamic therapy against cancer [42,43].

In 2008, Altinoglu et al. reported calcium phosphate nanoparticles (CPNPs) with encapsulated IcG for *in vivo* (nude mice) imaging of breast cancer (MDA-MB-231). In this work, the quantum efficiency of the CPNP-IcG was two-fold higher compared with free IcG, furthermore, the half-live of CPNP-IcG was about five times longer than the free IcG under clinical imaging conditions. These nanoplatforms also showed deeper signal detection and prolonged circulation compared with the photosensitizer alone [120]. Another study reported a decrease in the rate of elimination for indocyanine green when encapsulated in micelles for *in vivo* BALB/c nude mice model [121].

2.7. P22 nanoreactors

The design of P22 nanoreactors with CYP activity was first reported by Sánchez-Sánchez et al. in 2015. Scaffold protein of P22 procapsid was fused with CYP_{BM3}21B3 through recombinant DNA technology, obtaining a high concentration of CYP enzyme encapsidated.

Improved stability in acidic pH and protease resistance are unique characteristics of these nanoreactors. Because of their properties, they have potential use in enzyme prodrug therapy against cancer [44].

A recent study developed enzyme P22 nanoreactors for the transformation of endocrine disruptor compounds. Cytochrome P450 was encapsidated, and glucose oxidase was functionalized on the surface; a cascade system between CYP and GOx allows the transformation of endocrine disruptor compounds only in the presence of glucose (Figure 14). This study proposes the use of nanoreactors to eliminate toxic compounds from cells and tissues, and their potential use in enzyme-prodrug therapy [45].

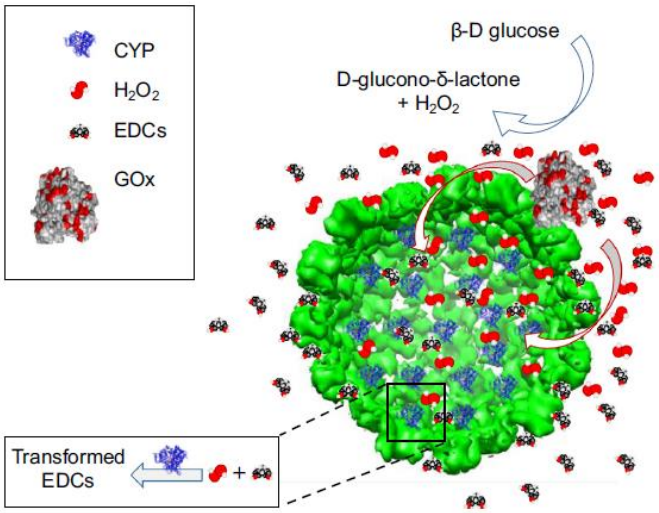

Figure 14. Representation of the P22 capsids with glucose oxidase and CYP used to transform endocrine disruptor compounds. Obtained from González-Davis et al. [45].

The multi-functionalization of P22 viral capsids with CYP activity was reported to treat breast cancer. CYP was fused with scaffold protein (SP) to allow the enzymatic activation of tamoxifen inside cancer cells; furthermore, the functionalization of protoporphyrin and estradiol-derivated compounds was used to reach a combination enzyme-photodynamic targeted therapy (Figure 15) [46].

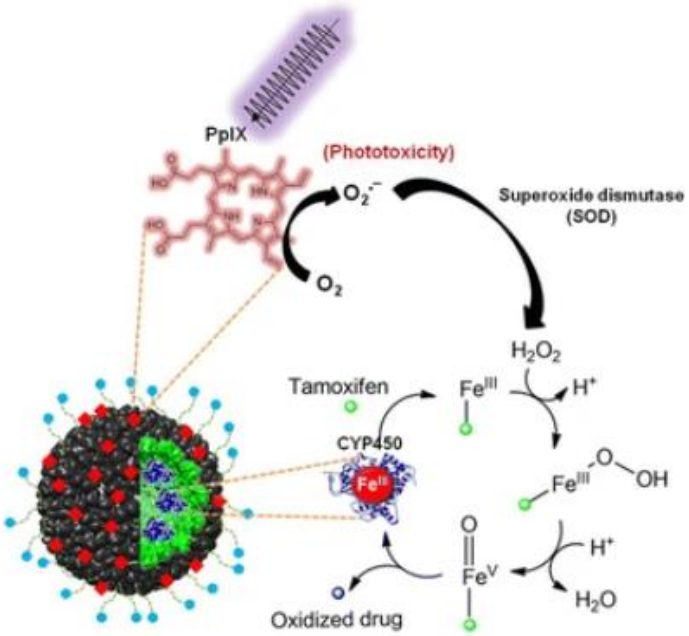

Figure 15. Schematic representation of the synergistic enzyme-prodrug and photodynamic therapy proposed by Chauhan et al. [46].

This study highlights the potential use of P22 nanoreactors as multimodality nanoplatforms with retained structural integrity. Furthermore, it is possible to use VLPs in combinatory therapy.

3. Justification, hypothesis, and objectives

3.1. Justification

Smart drug delivery systems responsive to tumor microenvironment [including cellular metabolism or the physical attributes (pH, redox species)] are desirable in clinical medicine due to their enhanced therapeutic efficacy and minimal adverse effects. Overall, the proposed project aims to develop P22 bacteriophage as multimodality therapeutic nanoreactors with combined function of glucose-mediated dual enzymatic activity and near infrared light-stimulated photodynamic therapy for smart action against breast cancer.

3.2. Hypothesis

Multi-functionalized bi-enzymatic P22 viral capsids can be used to reach a stimuli-responsive combination therapy for improved breast cancer treatment.

3.3. General objective

Optimize the enzyme co-immobilization strategy for effective cascade reaction with CYP and GOx enzymes in P22 viral capsids and functionalize these capsids with a photosensitizer to evaluate their potential for application in enzyme-prodrug, photodynamic, photothermal, and starvation therapies against breast cancer.

3.4 Specific objectives

- Purify P22-CYP viral capsids by fast protein liquid chromatography, characterize the amount of encapsulated CYP on the nanoreactors.

- Evaluate different reactions for the functionalization of GOx on the surface of the nanoreactors, characterize the combined enzyme kinetics.
- Functionalize IcG on the surface of the nanoreactors, characterize the generation of ROS and thermal properties under near-infrared excitation.
- Characterize the physicochemical properties after each functionalization step of the nanoreactors.

4. Methods

4.1 Purification and characterization of P22-CYP capsids

4.1.1. Ultracentrifugation and fast protein liquid chromatography (FPLC)

The core biocatalytic P22-CYP were obtained from the group of Dr. Vazquez-Duhalt as bacterial cell pellets produced from *E. coli* BL21(DE3) cells harboring the expression plasmids pBAD CYP-SP and pRSF P22 as reported by Sánchez-Sánchez et al. in 2015 [44]. The purification of the cell pellets containing P22 capsids fused with CYP_{BM3}21B3 from *Bacillus megaterium* had two main steps, protein extraction from bacterial cells, and the later purification by size exclusion chromatography.

The pellets were resuspended on 100 mL of lysis buffer (50 mM sodium phosphate, 100 mM NaCl, pH 7.6), and sonicated using an ultrasonic cell disruptor homogenizer (YM-1000Y, TOPTION) at 40% of power for 10 minutes, with 9.9 seconds of sonication and 9.9 seconds of pause. The lysed mixture was centrifuged with a fixed-angle rotor JA-25.50 (Beckman Coulter) at 13,000 rpm, 4°C for 45 minutes to remove cell debris. The supernatant was ultracentrifuged with a sucrose cushion [35% (w/v)] using the rotor SW 32 Ti (Optima XPN100 Ultracentrifuge, Beckman Coulter) at 31,000 rpm, 4°C for 2:15 hours. The resultant pellets were resuspended in PBS buffer (50 mM Na_2HPO_4, 25 mM NaCl, pH 7.4), filtrated with a 0.45 µm Millipore membrane, and purified with size exclusion column (HiPrep 16/60 Sephacryl S-500 HR, Sigma Aldrich) in a fast protein liquid chromatography (AKTA Prime Plus, General Electric). Prior to injection, the column was equilibrated with 4 column volumes of PBS buffer. The fractions containing the well-formed VLPs were collected and ultracentrifuged at 31,000 rpm, 4°C for 2:15 hours.

The purified pellets were resuspended in PBS buffer and stored at -80°C until further use. The purity of samples was established with gel electrophoresis and TEM.

4.1.2. Quantification of P22 viral capsids

Pierce BCA Protein Assay Kit (Thermo Fisher Scientific) was used to quantify the amount of protein in the purified capsids solution. The assay is based on the interaction of protein with reagent that leads to reduction of Cu^{2+} to Cu^{+} under alkaline conditions and the resultant complex shows absorption at 562 nm. Five different concentrations of the standard bovine serum albumin (BSA), and two different dilutions of the sample were tested in duplicate using the protocol given by the provider. After 30 min incubation of samples with reagent at 37˚C, the absorbance at 562 nm was measured using a UV-spectrometer (Multiskan GO, Thermo Scientific). A standard curve of BSA was plotted and the concentration of samples was estimated from the equation of straight line.

4.1.3. Densitometric analysis on SDS-PAGE gel

Required solutions for the SDS-PAGE electrophoresis were prepared. Acrylamide-bisacrylamide solution (30%-0.8%), Tris-HCl buffer (pH 8.8, 1.5 M), Tris-HCl buffer (pH 6.8, 0.5 M), 10% (w/v) ammonium persulfate (APS), running buffer 1x, staining solution (0.1% Coomassie), and loading buffer (0.1 mg/mL bromophenol blue, 0.05 mg/mL 2-Mercaptoethanol).

Separating gel at 12% was prepared using 3.5 mL of distilled water, 4 mL of polyacrylamide solution, 2.5 mL of Tris-HCl buffer (pH 8.8), 50 µL of APS (10%), and 10 µL of tetramethylethylenediamine (TEMED). The stacking gel was prepared with 3 mL of distilled water, 0.75 mL of polyacrylamide solution, 1.25 mL of Tris-HCl buffer (pH 6.8), 15 µL of APS (10%), and 6 µL of TEMED.

Three different concentrations of purified P22, a non-purified sample of P22, and the sample corresponding to the aberrant VLPs were run in the electrophoresis gel. The samples were mixed with loading buffer in 1:1 (v/v) ratio and heated at 95°C for 10 minutes before running the gel.

The samples were loaded to the gel and was run at 200 V for 1:30 hour. After the electrophoresis, the gel was first stained with the Coomassie solution, and then, distained to obtain the clear bands of protein. The gel was scanned in an SDS-PAGE gel transilluminator (iBright FL1000, Thermo Scientific). Finally, ImageJ software was used to perform the densitometric analysis and to calculate the ratio of CP and CYP-SP proteins.

4.1.4. Confinement molarity and percent occupancy

To calculate the confinement molarity and the percent occupation, equations 8 and 9 were used, as described for Tafoya Romo in 2017 [47].

$$M = \frac{(N_{enz})}{(V_{int})(N_A)} \quad \text{[Eq. 8]}$$

Where M is the confinement molarity, N_{enz} is the number of CYP enzymes per capsid, V_{int} is the internal volume of the capsid, and N_A is the Avogadro number.

$$\%Occupancy = \frac{(N_{enz})(V_{enz})(100)}{(V_{int})} \quad \text{[Eq. 9]}$$

Where N_{enz} is the number of CYP enzymes per capsid, V_{enz} is the volume of the CYP, and V_{int} is the internal volume of the capsid.

4.2. Multi-functionalization of the nanoreactors

4.2.1. Glucose oxidase functionalization

Four different crosslinking reactions under mild conditions were tested to functionalize glucose oxidase (GOx) from *Aspergillus niger* (Sigma Aldrich) on the surface of the capsid. One reaction using glutaraldehyde, second, using carbodiimide coupling with a combination of 1-ethyl-3-(3-dimethylaminopropyl)carbodiimide (EDC) and N-hydroxysuccinimide (NHS); and third and fourth with a four-component UGI reaction for dipeptide formation proposed by Ugi et al. in 1959 [48].

For the first reaction, 250 µg of glucose oxidase and 250 µg of P22 purified nanoreactors were mixed in PBS buffer (pH 7.4) with 0.1% (v/v) of glutaraldehyde. The solution was left in constant agitation for 2 hours.

The second reaction consisted of two steps; in the first step, 250 µg of glucose oxidase were mixed with 4.5 µg of EDC and 2.7 µg of NHS, to obtain a molar enzyme-compound ratio of 1:15. Glucose oxidase was left under agitation for 30 minutes and centrifuged at 8000 g (Multifuge X1R, Thermo Scientific) for 5 minutes in a 100 kDa membrane filter. For the second part, the glucose oxidase pellet was resuspended in a solution with 250 µg of P22 nanoreactors, 0.35 µg of EDC, and 0.21 µg of NHS to obtain an P22-compound molar ratio of 1:200. The solution was left two hours under constant agitation at room temperature.

For the last reaction, two molar ratios of P22-compound were used, 1:300 and 1:50. For the 1:300 molar ratio, 250 µg of P22 nanoreactors were mixed with 0.33 µg of formaldehyde and left five minutes under agitation. After that, 250 µg of glucose and 0.79 µg of *tert*-butyl isocyanide were added to the solution, the reaction was diluted to 100 µL and left under agitation for two hours at room temperature. For the second molar ratio (1:50) the same

methodology was used, this time adding 0.0574 μg of formaldehyde and 0.151 μg of *tert*-butyl isocyanide.

After each reaction, solutions were ultracentrifuged using a fixed angle rotor 90 Ti (Optima XPN1000, Beckman coulter) for 1:30 hour at 40,000 rpm, and 4°C. The obtained pellets were resuspended in PBS buffer pH 7.4.

4.2.2. Indocyanine green functionalization

One milligram of P22-CYP-GOx nanoreactors was used to functionalize indocyanine green (IcG). NHS and EDC were used in an enzyme-compound ratio of 1:150, and the reaction was left under agitation for 30 minutes at room temperature. After this step, indocyanine green was added in a 1:150 molar ratio (enzyme-IcG) and left under agitation for 2 hours. The excess IcG was removed by centrifugation (Multifuge X1R, Thermo Scientific) using 100 kDa membrane filters at 8000 g for 5 minutes and 4°C; this centrifugation step was made twice for washings with PBS.

4.3. Enzyme activity of P22 nanoreactors

4.3.1. Enzyme activity of glucose oxidase

To corroborate the presence of glucose oxidase in the nanoreactors, a GOx enzyme activity was performed. The reaction medium was composed of sodium acetate buffer (50 mM, pH 5.1), dextrose (4.75 mM), and guaiacol (0.8 mM). To start the reaction, 957 μL of the reaction medium were mixed with 10 μL of the functionalized nanoreactors, and 33 μL of peroxidase with an activity of 60 U/mL. The GOx undergoes glucose oxidation and produces H_2O_2 as a side product, which is used by HRP for guaiacol oxidation (ε_{470} = 26,600 M^{-1} cm^{-1}) [49]. The absorbance of oxidized guaiacol was monitored at 470 nm for 2 minutes using a UV-Vis spectrometer (Lambda 25, Perkin Elmer) to calculate the enzyme activity.

4.3.2. Enzyme activity of cytochrome P450

The reaction medium for the CYP activity assay contained 2,6-dimethoxyphenol (DMP) (500 µM), and Tris-HCl buffer (pH 8, 50 mM). To start the reaction, 985 µL of reaction medium were mixed with 10 µL of P22 nanoreactors, and 5 mM of H_2O_2 in a final volume of 1 mL. Immediately after the addition of hydrogen peroxide, the absorbance of the solution was monitored using a UV-spectrometer (Lambda 25, Perkin Elmer) at 468 nm for 5 minutes. The molar extinction coefficient of the transformed product of DMP at 468 nm is 14,800 $M^{-1}cm^{-1}$ [50].

To determine the kinetic parameters of the cytochrome P450 in the P22-CYP nanoreactors, enzyme activity assays were performed with different concentrations of DMP. Obtained data was processed using GraphPad Prism 8.0.1 software to calculate the kinetic parameters.

4.3.3. Cascade enzyme activity of CYP

To measure the combined activity of CYP and GOx, the reaction medium contained Tris-HCl buffer (pH 8, 50mM), DMP (500 µM), and glucose (95 µM). 950 µL of the medium were mixed with 50 µL of the functionalized nanoreactors, and the absorbance was monitored for 45 minutes at 468 nm using a UV-spectrometer (Lambda 25, Perkin Elmer). The molar extinction coefficient of DMP transformation product at 468 nm is 14,800 $M^{-1}cm^{-1}$ [50].

Nanoreactors functionalized in each step were used to determine the kinetic parameters of the GOx and CYP combined activity. Different concentrations of glucose were used in the enzyme assays, and the obtained data was processed using GraphPad Prism 8.0.1 software to calculate the kinetic parameters.

4.4. Photophysical properties after IcG functionalization

4.4.1. Quantification of indocyanine green on the nanoreactors

Five different concentrations (0.1 to 0.5 µg/mL) of IcG diluted in PBS buffer were used to obtain a calibration curve, the maximum absorbance at 790 nm of the solutions was measured by triplicate using a UV-Vis spectrometer (Lambda 25, Perkin Elmer). The same absorbance was measured in a diluted concentration of the nanoreactors to estimate the concentration of the functionalized IcG.

4.4.2. Absorption and fluorescence of the nanoreactors

Fluorescent blot imaging system (iBright FL1000, Thermo Fisher Scientific) was used to obtain the images of sample fluorescence after functionalization of IcG. Excitation and emission wavelength were adjusted to 745-760 and 810-850 nm respectively. Eppendorf tubes with PBS buffer, P22-CYP-GOx, and P22-CYP-GOx-IcG nanoreactors were scanned with an exposure time of 1326 ms.

The absorption spectrum of the nanoreactors in each functionalization step was obtained using a UV-spectrometer (Lambda 25, Perkin Elmer), the absorbance was measured from 300 to 1000 nm with the same concentration of protein in all samples.

4.4.3. Fluorometric reactive oxygen species assay

The ROS generation assay was performed monitoring the degradation of 1,3-diphenylisobenzofuran (DPBF) in a fluorescence spectrophotometer (Cary Eclipse, Agilent Technologies). For the assay, 38 µg of the IcG-functionalized nanoreactors (0.11 µg of IcG) were mixed with DPBF (10 µM) and DMSO in a final volume of 200 µL. This solution was irradiated with an 808 nm laser (0.5 W) in intervals of two minutes for a total exposure time

of 12 minutes; after each interval, the emission fluorescence spectrum was obtained using 410 nm for the excitation wavelength.

4.4.4. Thermal properties

The change in the temperature of the nanoreactors under near-infrared light was monitored using a digital source (FOB100, Omega) coupled to an optical fiber temperature sensor. 377 µg of IcG-functionalized nanoreactors (1.07 µg of IcG) were diluted in 100 µL of PBS buffer and irradiated with an 808 nm laser (0.5 W) for 5 minutes, the temperature of the nanoreactors was measured in 20 seconds intervals. PBS buffer was used as a control for this experiment.

4.5. Size distribution and zeta potential of nanoreactors

4.5.1. TEM characterization

P22-CYP-GOx nanoreactors were analyzed using a Transmission Electron Microscope (JEM-2010, JEOL). The voltage was set at 80 kV and the sample preparation was performed by staining the sample with 5 µL of 2% uranyl acetate for 2 min. The size distribution of the nanoreactors was obtained using ImageJ software.

4.5.2. DLS size distribution and Z potential

Dynamic Light Scattering (DLS) was used to obtain the size distribution and Z potential of the nanoreactors at different stages of functionalization. 10 µg of nanoreactors were diluted in 500 µL of PBS to perform the characterization in DLS (Zetasizer Nano ZS, Malvern Panalytical), the measurements were done in triplicate.

5. Results

5.1. Purification and characterization of P22-CYP capsids

5.1.1. Purification of P22-CYP capsids

To collect the viral capsids avoiding damage by mechanical stress, the capsids were centrifuged in a sucrose cushion. After this, a size exclusion chromatography was performed, and the absorbance of the fractions was monitored at 280 nm. The elution profile of the fractions showed two main peaks at 55 and 70 minutes (Figure 16). 30 fractions of 2 mL were collected from minutes 48 to 108.

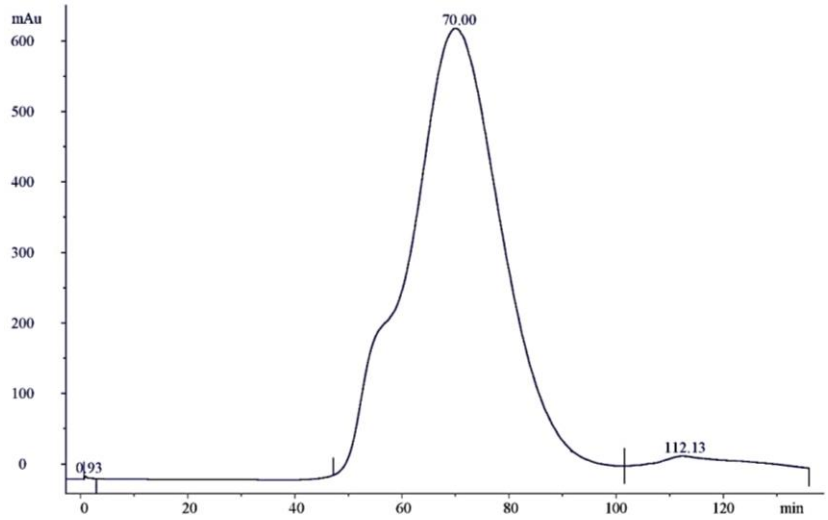

Figure 16. Elution profile of the P22 viral capsids with CYP activity obtained by size exclusion chromatography. Two main peaks are observed at 55 and 70 minutes.

In a previous work, Tapia, M. reported two peaks at 47 and 59 minutes corresponding to the aberrant and the correctly assembled P22 viral capsids respectively [51]. A more recent study

by Tafoya, P. in 2017 showed two peaks at 55 and 65 minutes corresponding to the aberrant and well-formed capsids respectively [47]. In the present work, two similar peaks were observed at 55 and 70 minutes. CYP enzyme activity was measured in different fractions (Table III) to collect the capsids with the highest enzyme activity.

Table III. Cytochrome P450 enzyme activity obtained in different FPLC fractions.

Fraction	Elution time (min)	ΔAbs/min
8	62	0.034
9	64	0.047
10	66	0.118
15	76	0.072
17	80	0.051

The initial slope (Abs/min) is proportional to the enzyme activity of the CYP, thus fractions corresponding to 66 - 78 elution times were mixed because of their maximum enzymatic activity. Those were the fractions of the second peak obtained in the FPLC, and according to previous studies, this peak corresponds to the elution of well-assembled viral capsids [47,51].

5.1.2. Quantification of protein in P22 viral capsids

Pierce BCA protein assay kit (Thermo Fisher Scientific) was used to quantify the concentration of protein in the P22 aliquots after purification. The absorbance was measured at 562 nm in 1:30 and 1:50 dilutions. With the equation of the calibration curve ($R^2 = 0.99$), and considering the dilutions, the obtained concentration of protein in the aliquots was 7.361 ± 0.768 mg/mL.

5.1.3. Densitometric analysis of proteins on SDS-PAGE gel

Densitometric analysis of SDS-PAGE gel was used to quantify the number of coat proteins (CP) per scaffold protein fused with CYP (CYP-SP) in the viral capsids. Three different

concentrations of the capsids, a non-purified sample, and a sample of aberrant VLPs were run in the gel (Figure 17).

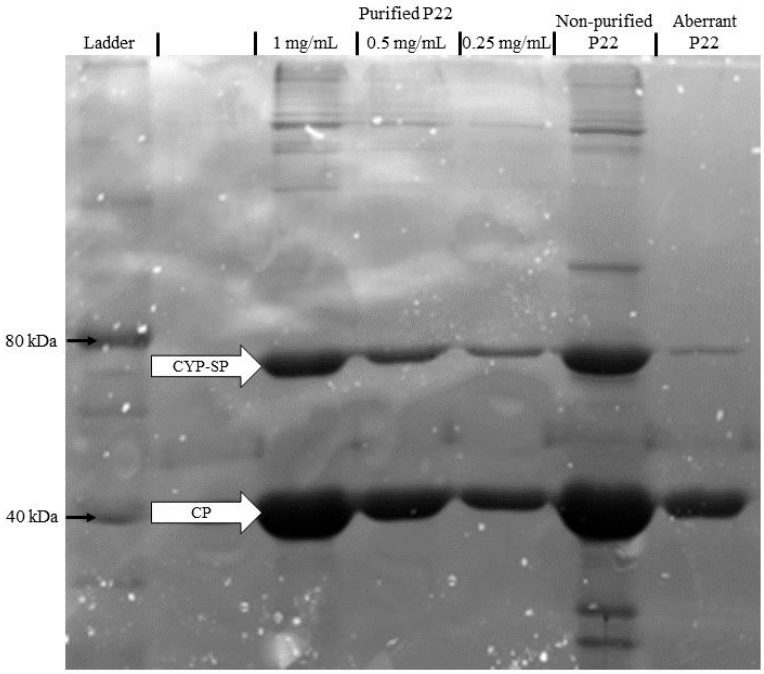

Figure 17. SDS-PAGE gel with P22 viral capsids samples. Purified, non-purified, and aberrant P22-CYP capsids were run in the electrophoresis gel.

The successful purification of P22 capsids was corroborated because CP and CYP-SP are by far the most important bands in the gel, nevertheless, some residues with about 160 kDa were visible in the highest concentration of the purified capsids. CP and CYP-SP have a reported molecular weight of 46.6 and 71.5 kDa respectively [50]. ImageJ software was used to obtain the area ratio for the bands corresponding to CP and CYP-SP and calculate the number of CYP-SP per CP proteins (Table IV).

Table IV. Densitometric analysis to calculate CP and CYP-SP ratio.

Sample	**CP: CYP-SP ratio**	**Number of proteins CP: CYP-SP**	**Molecular weight (MDa)**
Purified P22	2.5: 1	420: 110	27.44
Non-purified P22	2.6: 1	420: 105	27.08
Aberrant P22	4.7: 1	420: 58	23.72

Auto-assembly of P22 capsids requires 420 coat proteins and about 100 to 300 scaffold proteins [22]. To calculate the number of CP per CYP-SP, the number of CP was fixed at 420, and the number of CYP-SP was calculated assuming that the area of the proteins in the gel is proportional to their amount, i.e. in mg.

P22 capsids with 110 CYP-SP proteins were obtained after the purification, similar studies showed the encapsidation of 109 and 92 CYP enzymes per P22 capsid [44,45]. The first peak of the FPLC showed structures with about 58 CYP-SP molecules per capsid, and according to Zlotonic et al., 2016, a lower concentration of SP leads to the formation of aberrant structures [52].

5.1.4. Confinement molarity and percent occupancy

Equations 8 and 9 were used to calculate the confinement molarity and the percent occupancy of CYP inside the capsid.

$$M = \frac{(N_{enz})}{(V_{int})(N_A)} = \frac{110\ enzymes}{(55400\ nm^3)(N_A)} = 3.29\ mM \qquad \text{[Eq. 8]}$$

According to the SDS-PAGE densitometric analysis, there were 110 CYP-SP proteins per capsid. The internal volume was obtained with the TEM size distribution analysis, where the mean internal diameter was 47.3 nm, equivalent to a volume of 55,400 nm^3. The estimated confinement molarity of CYP in the viral capsid was 3.29 mM. This result is similar to the obtained by Tapia Moreno et al., 2017, where they encapsidated 109.7 CYP enzymes per P22 capsid, obtaining a confinement molarity of 3.14 mM [50].

$$\%Occupancy = \frac{(N_{enz})(V_{enz})(100)}{(V_{int})} = \frac{(110\ enzymes)(150\ nm^3)}{(55240\ nm^3)} = 29.9\% \qquad \text{[Eq. 9]}$$

The percent occupancy was calculated using 3.3 nm as the hydrodynamic radius of the CYP, obtaining an enzyme volume of 150 nm^3 [44]. With this CYP volume, the obtained occupancy was 29.9%.

5.2. Photophysical properties of the nanoreactors

5.2.1. Absorbance and fluorescence of the nanoreactors

To corroborate the functionalization of IcG, the absorption spectra after each functionalization step of the nanoreactors were obtained. The nanoreactors were diluted in PBS with similar concentrations and their absorbance was monitored from 300 to 1000 nm (Figure 18).

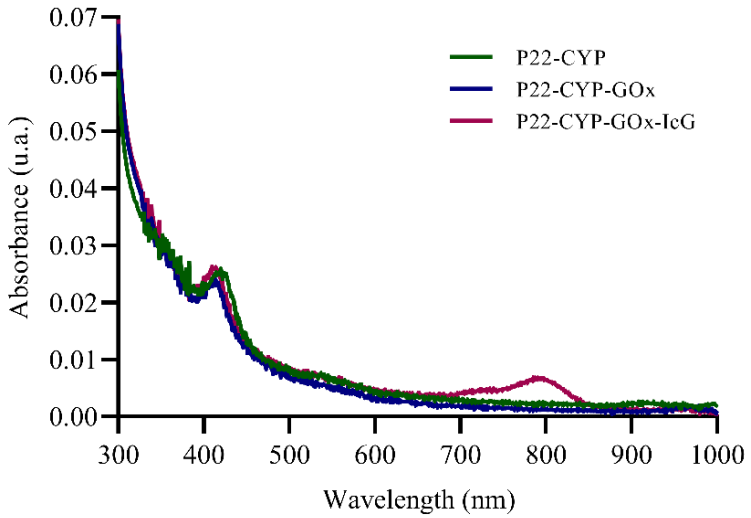

Figure 18. Absorption spectra of the nanoreactors. Nanoreactors functionalized with indocyanine green showed a characteristic absorption peak of IcG between 700 and 850 nm.

According to Landsman et al., depending on the solvent that is used and the concentration of IcG, the absorbance can vary from 600 to 900 nm. In diluted aqueous solutions, indocyanine

green has its maximum absorbance and fluorescence emission at 780 and 830 nm respectively [57,58].

All the nanoreactors exhibited a similar absorption profile, with the exception of P22-CYP-GOx-IcG nanoreactors that showed an increase of the absorbance between 700 and 850 nm. On the other hand, the additional absorption peak at Soret region (~410 nm) corresponds to the heme group of CYP.

The fluorescent blot imaging system was used to corroborate the fluorescence of the nanoreactors, excitation wavelengths were adjusted at 745-760 nm and emission wavelengths were monitored at 810-850 nm. Positive control of IcG and negative controls containing P22-CYP-GOx nanoreactors and PBS buffer were used (Figure 19).

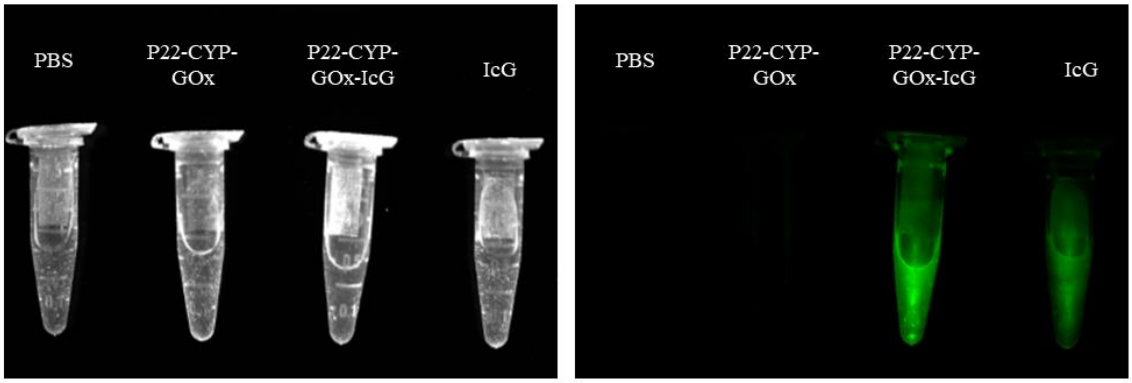

Figure 19. Near-infrared fluorescence in different samples with PBS buffer, P22-CYP-GOx and P22-CYP-GOx-IcG nanoreactors, and IcG diluted in PBS. The figure shows the control (left) and emission fluorescence (right).

The obtained image showed that only the Eppendorf tubes with IcG and P22-CYP-GOx-IcG nanoreactors exhibited fluorescence at 810-850 nm; therefore, the functionalization of indocyanine green in the nanoreactors was confirmed due to the presence of these characteristic absorption peak and fluorescence emission.

5.2.2. Indocyanine green quantification

To quantify the concentration of IcG in the nanoreactors, a calibration curve was made measuring the absorbance at 790 nm for different concentration of indocyanine green diluted in PBS buffer. The absorbance of a 50x dilution of the nanoreactors was further measured at 790 nm to calculate the IcG concentration (Figure 20).

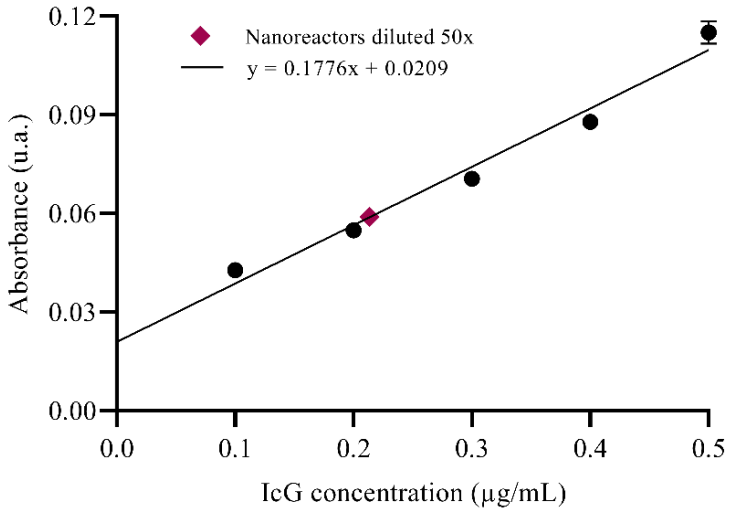

Figure 20. Calibration curve of indocyanine green used to calculate the concentration of functionalized ICG on the surface of nanoreactors. The purple diamond represents the absorbance of a 50x dilution of the P22-CYP-GOx-IcG nanoreactors.

Using the equation obtained from the calibration curve, and considering the dilution of the nanoreactors, the concentration of IcG in the nanoreactors was 10.689 µg/mL, corresponding to 2.84 µg of IcG per mg of nanoreactors. Considering the molecular weight of the compounds, it was estimated that 101 molecules of IcG were functionalized per nanoreactor. A study by Shemesh et al., 2104, found that 12 µg/mL of IcG carried by liposomes was enough to reduce the cell viability up to 60% under irradiation with an 808 nm laser in HCC1806 (human breast cancer) cells [59].

5.2.3. ROS generation assay

The generation of reactive oxygen species (ROS) by conjugated IcG was confirmed by qualitative monitoring the change in fluorescence intensity of ROS sensitive dye, 1,3-diphenyl isobenzofuran (DPBF) after NIR irradiation. The DPBF reacts with ROS and undergoes transformation to form non-fluorescent 1,2-dibenzoylbenzene (DBB). Thus, a decrease in fluorescence intensity is seen with the increase in time irradiation. Briefly, the nanoreactors with 2.84 µg/mg concentration were mixed with DPBF (10 µM). The reaction mixture was irradiated with an 808 nm laser (0.5 W) in 2 minutes intervals to observe the fluorescence at the excitation wavelength of 410 nm (Figure 21).

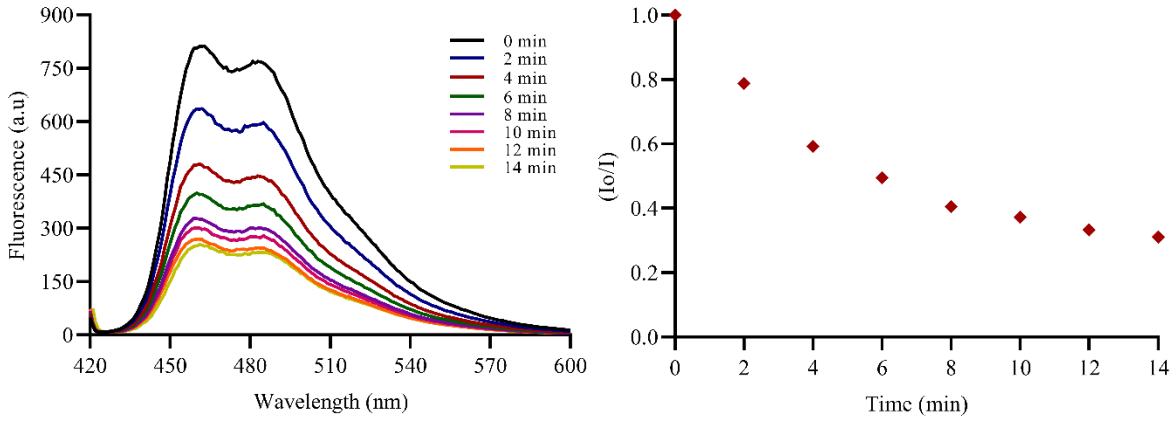

Figure 21. Fluorometric ROS production assay of the nanoreactors monitoring the conversion of DPBF. (left) Change in the fluorescence intensity after irradiation under an 808 nm laser. (right) Normalized decrease of the fluorescence.

A decrease in the fluorescence of DPBF is related to an increase in the generation of singlet oxygen and superoxide molecules [60,61]; moreover, a recent study confirmed the generation of ROS just by measuring the decrease in the fluorescence of DPBF in polymer nanoparticles functionalized with IcG [62].

The fluorescence decrease showed a first order decay with a pseudo-linear behavior between 0 to 4 minutes. After 6 minutes of irradiation, DPBF retained 50% of its initial fluorescence, and by the end of the experiment, about 35% of fluorescence was retained. Overall, the

analysis suggests the generation of singlet oxygen and superoxide due to the excitation of IcG under near-infrared light.

5.2.4. Temperature change of nanoreactors

As described earlier, IcG produces heat after irradiation at excitation wavelength. Thus, the temperature change of P22-CYP-GOx-IcG nanoreactors was monitored under near-infrared irradiation (808 nm) every 20 seconds for 5 minutes. The 377 µg of nanoreactors diluted in 100 µL were used in this experiment with total IcG concentration as 10.69 µg/mL. The cumulative change in the temperature was calculated along with its respective control (Figure 22).

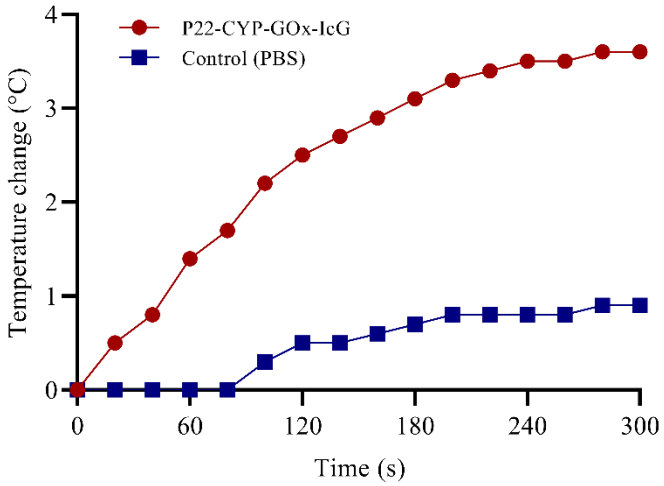

Figure 22. (Red) Cumulative change in the temperature of P22-CYP-GOx-IcG nanoreactors under near-infrared light. (Blue) Cumulative change in the temperature of control with PBS buffer under near-infrared light (0.5 W).

Photothermal therapy (PTT) consists of the use of near-infrared (NIR) laser and NIR absorber compounds to transform the light into heat, increasing the temperature at cellular environment, and causing several damages to the proteins and cell membrane [36]. In this case, the functionalized IcG in the nanoreactors is a photosensitizer that is excited with NIR radiation and starts a heating process, raising the temperature of the medium up to 3.6°C in 5 minutes.

Different studies using nanoplatforms to carry IcG in similar concentrations as P22-CYP-GOx-IcG nanoreactors have shown an increase in the temperature at the first two minutes under NIR irradiation from 15 to 20°C [63-66].

It is to be noted that the laser power in most of the reported studies is 1-1.5 W, however, the power of laser used in our experiment was 0.5 W, which is half the power of lasers used in other studies. Thus, the change of the temperature cannot be directly compared between studies because factors such as the power density of the laser (W/cm^2) and the type of nanocarriers used can enhance the thermal properties of the indocyanine green. Nevertheless, the photothermal efficiency of P22-CYP-GOx-IcG can be further improved by using high power laser.

Hyperthermia is the process of raising the temperature in tumors in order to kill cancer cells, *in vitro* studies usually require temperatures above 41 or 42°C depending on the cell lines to significatively reduce cell viability [67,68]. Theriault et al., 2012 reported that MDA-MB-231 (breast cancer) cells stopped its growth after 72 hours at 41°C and started to decrease its viability above this temperature [69]. Another study by Thompson et al. reported a decrease in cell viability from 60 to 80% in different breast cancer cell lines (MCF-10A, MCF-7, and MDA-MB-231) after 5 minutes at 40°C [70].

5.3. Physicochemical properties of the nanoreactors

5.3.1. Size distribution and zeta potential

Size distribution and zeta potential of the nanoreactors were measured by DLS after each functionalization step (Figure 23, Table V).

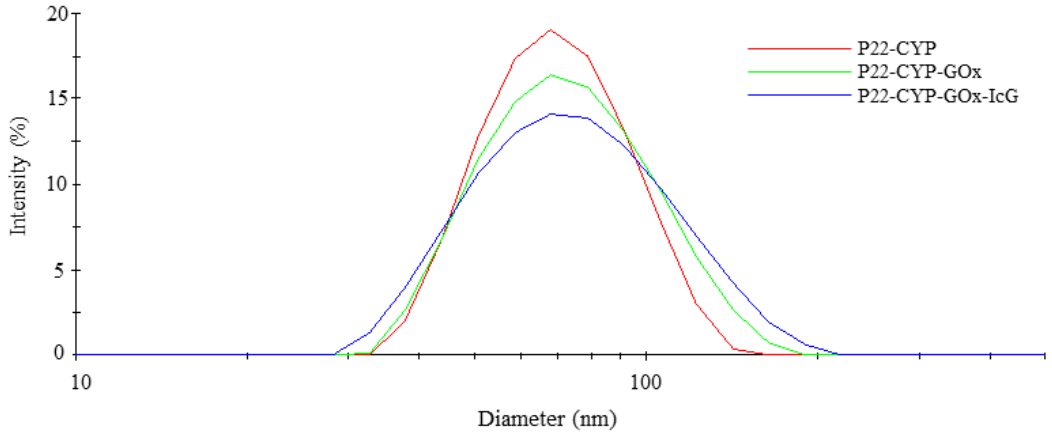

Figure 23. Size distribution for intensity of the functionalized nanoreactors. The mean hydrodynamic diameter tends to increase after each functionalization.

The size intensity distribution of the nanoreactors showed an increase in the hydrodynamic diameter after each functionalization step, furthermore, with every functionalization, the size distribution tended to get wider.

Table V. Zeta potential after each functionalization step.

Sample	Mean diameter (nm)	Zeta potential (mV)
P22-CYP	72 ± 20	-26 ± 10
P22-CYP-GOx	76 ± 26	-28 ± 10
P22-CYP-GOx-IcG	79 ± 31	-25 ± 11

Glucose oxidase is an enzyme with a hydrodynamic diameter of 8.6 nm [72], after its functionalization, there was an increase in the diameter of 4 nm. With the subsequent functionalization of IcG, the nanoreactors increased their diameter 3 nm. Zeta potential of the nanoreactors after the functionalization of each compound was almost the same.

Although DLS results did not clearly show a successful characterization, the presence of combined enzyme activity, and the fluorescence and absorbance of the nanoreactors was characterized to confirm the functionalization of GOx and IcG.

5.3.2. TEM characterization

The morphology of P22-CYP-GOx nanoreactors were analyzed using transmission electron microscope (TEM). (Figure 24). The micrographs were processed in ImageJ to obtain a size distribution histogram of the nanoreactors (Figure 25).

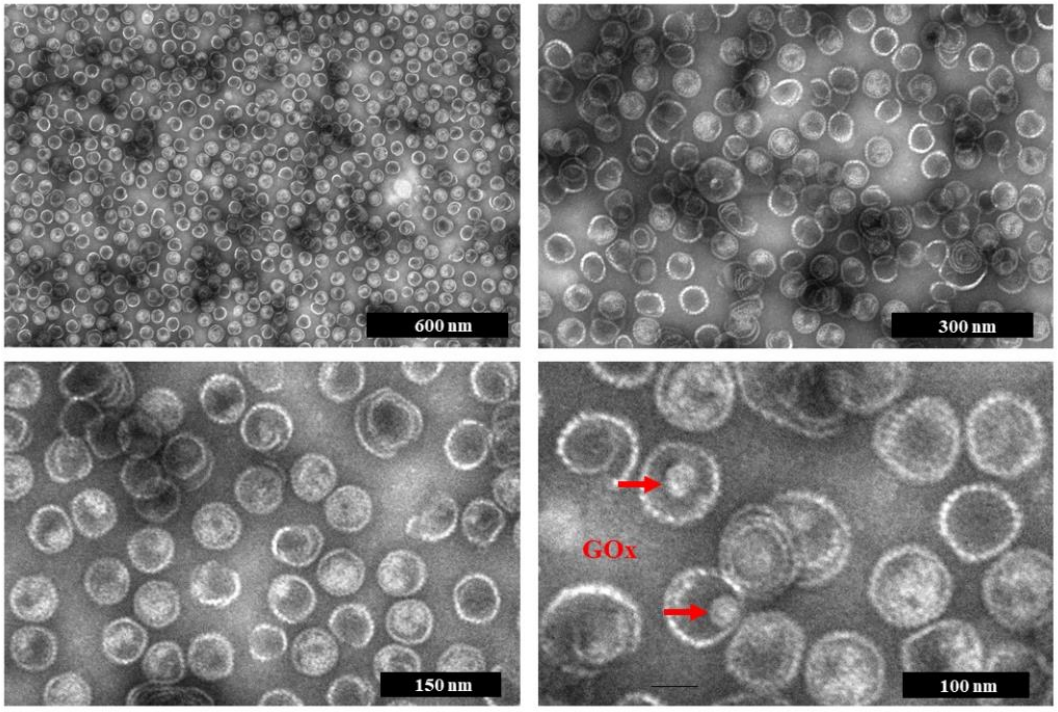

Figure 24. TEM micrographs of P22-CYP-GOx nanoreactors at different magnifications. Glucose oxidase is observed in some of the nanoreactors.

In general, most of the nanoreactors showed an icosahedral geometry, which is consistent with the reported geometry of the procapsid [71]. Bigger aberrant structures and open capsids were similar to those reported by Zlotonic et al. in 2012 due to the absence of scaffold protein and the subsequent polymerization of the coat proteins [52]. Glucose oxidase was found in some nanoreactors, which verified its successful functionalization.

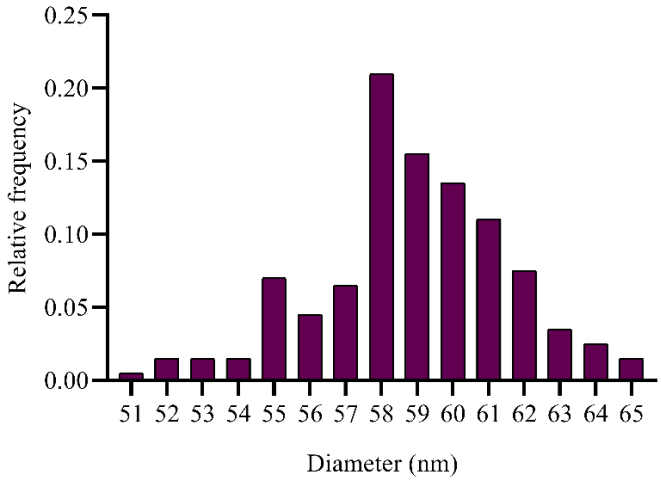

Figure 25. Size distribution of the nanoreactors by TEM analysis. The nanoreactors were monodispersed with a mean diameter of 58.75 nm.

The nanoreactors presented a monodisperse size distribution with a mean diameter of 58.75 ± 2.9 nm. This diameter is slightly different from the reported for other P22-CYP capsids, where the mean diameter was 53.6 and 53.8 nm [44,45]; nevertheless, this value is similar to the reported for the P22 procapsid structure [22].

5.4. Enzyme activity of the nanoreactors

The behavior of the enzyme kinetics was adjusted using the Michaelis-Menten model. V_{max} is expressed in terms of U/mg, corresponding to the number of substrate micromoles converted per milligram of protein in the nanoreactors per minute. On the other hand, the turnover number is expressed in units of time, corresponding to the number of substrate molecules converted per nanoreactor per minute.

5.4.1. CYP enzyme kinetics of P22-CYP capsids

To characterize the enzyme kinetics of P22-CYP nanoreactors, the cytochrome P450 activity was measured using different concentrations of DMP and keeping constant the H_2O_2 concentration (Figure 26).

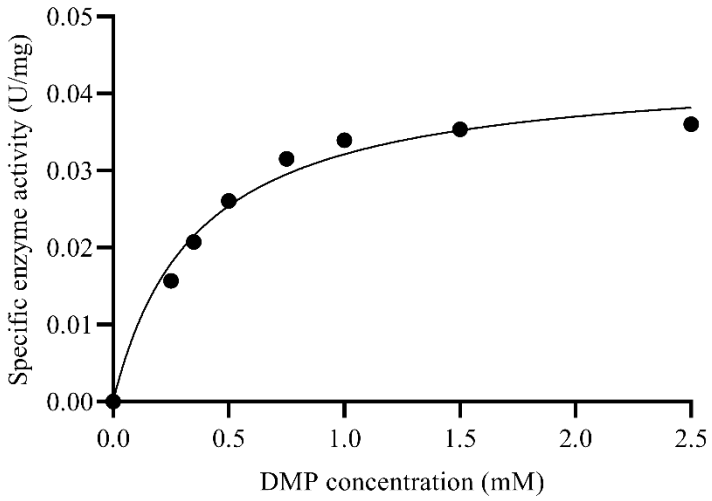

Figure 26. CYP enzyme kinetics of the P22-CYP nanoreactors. A Michaelis-Menten model was adjusted to the experimental data.

The experimental data was analyzed using Prism GraphPad 8.0.1 to adjust a Michaelis-Menten curve and calculate the kinetic constants V_{max}, K_M, and k_{cat} (Table VI).

Table VI. Kinetic constants of the CYP in P22-CYP nanoreactors.

	V_{max} (U/mg)	**K_M (mM)**	**k_{cat} (min^{-1})**
P22-CYP	0.04366	0.36	1198

- *Note:* In V_{max}, U represents the enzyme unit, defined as the amount of enzyme that catalyzes the transformation of 1 µmol of substrate per minute.

The maximum velocity of the nanoreactors was 0.04366 U/mg, which is equivalent to the conversion of 1198 molecules of substrate per minute per nanoreactor. This confirmed the CYP activity of the nanoreactors using H_2O_2 as the final electron acceptor.

5.4.2. Enzyme activity after each reaction for GOx functionalization

Note: *From this point, each reaction used to functionalize GOx will have a key name. The reaction with 0.1% of glutaraldehyde will be named "GHD", the one that used EDC and*

NHS will be "EDC-NHS", and the four component reactions [48] will be named "UGI 300" and "UGI 50" corresponding to the molar ratio used.

To corroborate the successful functionalization of glucose oxidase, GOx enzyme activity assay was performed with P22-CYP-GOx nanoreactors obtained after each reaction. The estimation of the amount of immobilized GOx on P22 surface was done by assuming same specific activity of free and functionalized enzyme (Table VII).

Table VII. Glucose oxidase activity after each reaction of GOx functionalization.

Reaction	GOx activity (U/mg)	Functionalized GOx (µg/mg)
GHD	0.0876	1.1426
EDC-NHS	0.2089	2.7256
UGI 50	0.3882	5.0066
UGI 300	0.5482	7.1544

- In the second column, U represents the enzyme unit, defined as the amount of enzyme that catalyzes the transformation of 1 µmol of substrate per minute.
- The third column is in terms of µg of functionalized GOx per mg of P22.

UGI 300 nanoreactors showed by far the highest GOx activity, followed by UGI 50 and EDC-NHS nanoreactors. GHD nanoreactors only showed 17% of the activity compared with the UGI 300. Glucose oxidase activity is proportional to the amount of enzyme functionalized, therefore, UGI reactions have the highest concentration of glucose oxidase of all the nanoreactors. The number of GOx enzymes functionalized was estimated, obtaining 0.2, 0.47, 0.87, and 1.23 GOx enzymes per GHD, EDC-NHS, UGI 50, and UGI 300 nanoreactor respectively.

For a better understanding of the nanoreactors after each reaction, the CYP specific activity was determined in all the nanoreactors to compare its activity with a control of P22-CYP capsids (Table VIII).

Table VIII. Cytochrome P450 specific activity after each reaction of GOx functionalization.

Reaction	CYP specific activity (U/mg)	Retained activity (%)
GHD	0.0255	41
EDC-NHS	0.0616	99
UGI 50	0.0562	91
UGI 300	0.0225	36
P22 without GOx	0.0618	100

- *Note:* In V_{max}, U represents the enzyme unit, defined as the amount of enzyme that catalyzes the transformation of 1 µmol of substrate per minute.

EDC-NHS and UGI 50 are the only two reactions that retained more than 90% of the original CYP activity of the P22-CYP nanoreactors. UGI 50 and GHD nanoreactors retained about 40% of the original CYP activity.

The lowest GOx and CYP activities of the GHD nanoreactors could be explained because extensive crosslinking with glutaraldehyde is known to cause distortion of the enzyme structure, obstructing the accessibility of the substrate and reducing the catalytic activity [53,88]. From another perspective, glutaraldehyde can react with all the primary amines in the solution, possibly causing agglutination between P22-CYP nanoreactors, affecting the diffusion rate of the substrates inside the capsids and modifying the enzyme kinetics [44,54].

Finally, the combined activity of GOx and CYP was measured using glucose as the substrate (Figure 27). The combination of GOx and CYP at the same nanoplatform is a smart approach where GOx undergoes glucose oxidation producing H_2O_2, which participates in the electron transfer mechanism of CYP for substrate transformation.

This combined enzyme activity is the most important, as one of the objectives is to achieve a cascade reaction between GOx and CYP mediated by glucose that is found in excess at cancer sites [77]. Thus, a self-activated prodrug transformation can be achieved specifically at the tumor region.

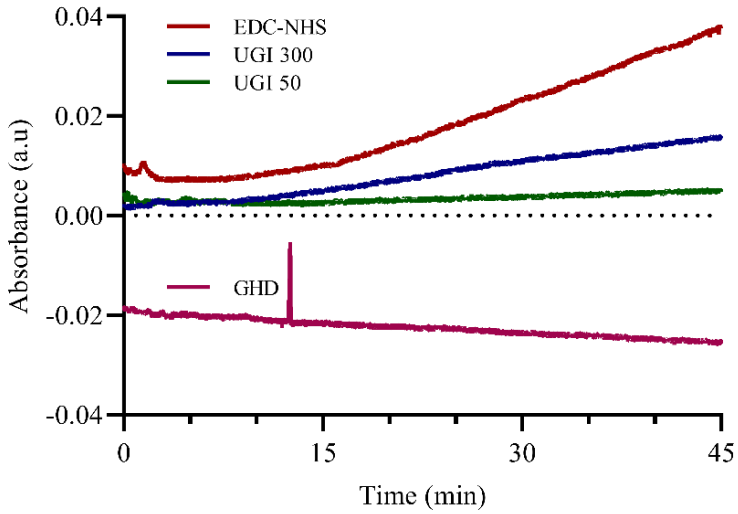

Figure 27. Combined enzyme activity of the nanoreactors after the functionalization of GOx with different reactions.

EDC-NHS synthesized nanoreactors showed higher activity than the ones functionalized with UGI reactions; on the other hand, GHD nanoreactors did not present combined activity, despite they presented individual CYP and GOx activity. The specific activity of CYP by cascade reaction was calculated for the three reactions (Table IX).

Table IX. Specific activity of CYP by glucose mediated cascade reaction.

Reaction	**Combined specific activity (U/mg)**
EDC-NHS	0.00258
UGI 50	0.00167
UGI 300	0.00162

- *Note:* In V_{max}, U represents the enzyme unit, defined as the amount of enzyme that catalyzes the transformation of 1 µmol of substrate per minute.

EDC-NHS nanoreactors have 55% more specific activity than the other ones. Possibly, the lower combined activity of UGI nanoreactors is caused by the high molar ratio of the reaction components, which leads to an extensive crosslinking, causing the distortion of the tertiary structure of enzymes and slowing the diffusion rate of substrates and products, thus modifying the kinetic parameters [55,89].

Because of their highest combined activity, the combined enzyme kinetics of EDC-NHS and UGI 50 nanoreactors was subsequently characterized.

5.4.3. GOx-CYP combined enzyme kinetics of UGI 50 and EDC-NHS nanoreactors

Combined enzyme kinetic was performed by varying the glucose concentration in the solution from 0 to 12 mM (Figure 28).

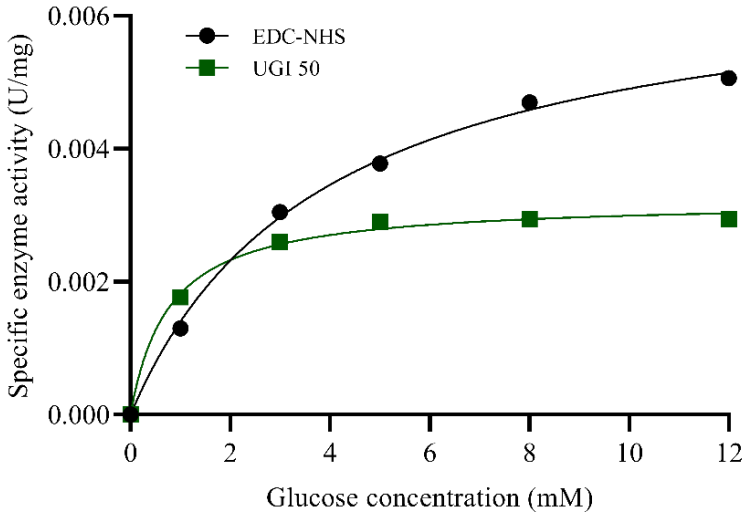

Figure 28. Transformation kinetics of DMP by the glucose-mediated cascade reaction using UGI 50 and EDC-NHS nanoreactors. Different concentrations of glucose were used to determine the Michaelis-Menten curve of the nanoreactors.

Michaelis-Menten curves of the combined enzyme activity were processed in GraphPad Prism 8.0.1 to calculate the maximum velocity (V_{max}), the Michaelis-Menten constant (K_M), and the turnover number (k_{cat}) of the nanoreactors (Table X).

Table X. Enzyme kinetic constants for DMP transformation by UGI 50 and EDC-NHS nanoreactors.

Reaction	**V_{max} (U/mg)**	**K_M (mM)**	**k_{cat} (min^{-1})**
UGI 50	0.00322	0.77	88
EDC-NHS	0.00681	3.88	187

- *Note:* In V_{max}, U represents the enzyme unit, defined as the amount of enzyme that catalyzes the transformation of 1 µmol of substrate per minute.

EDC-NHS nanoreactors exhibited two-fold the maximum velocity than the UGI 50, being capable of convert 187 molecules of substrate per nanoreactors per minute. However, the K_M constant of UGI 50 nanoreactors was almost 5 times smaller.

Human breast cancer cells MCF-7 in the absence of glucose supply, have intracellular glucose levels of 2.69 ± 1.47 mM, and some of them can reach concentrations of 7.11 mM [56]. It is widely known that cancer tumor requires higher concentrations to proliferate [126,127] At these high concentrations of glucose (>5.5 mM), EDC-NHS nanoreactors show a higher combined specific activity, therefore, they were used for further experiments.

5.4.4. Combined enzyme kinetics of the nanoreactors after IcG functionalization

Note: *Because of its highest V_{max}, EDC-NHS nanoreactors were used for the functionalization of the indocyanine green and further characterization after this point in the thesis.*

Indocyanine green was functionalized on P22-CYP-GOx through carbodiimide coupling to endow the properties useful for photodynamic and photothermal therapy. After the functionalization of indocyanine green, the combined enzyme kinetics were obtained by varying glucose concentration from 0 to 12 mM (Figure 29).

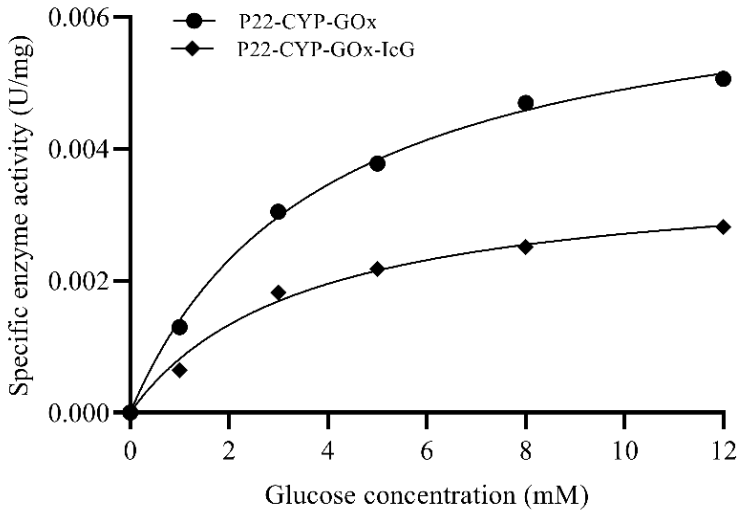

Figure 29. Transformation kinetics of DMP by glucose mediated cascade reaction using nanoreactors before and after IcG functionalization. The V_{max} of the nanoreactors decreased in IcG-functionalized nanoreactors.

The kinetics Michaelis-Menten curve showed a reduction in the combined specific enzyme activity after IcG functionalization. GraphPad Prism 8.0.1 was used to calculate V_{max}, K_M, and k_{cat} of the nanoreactors (Table XI).

Table XI. Catalytic constants for DMP transformation using the nanoreactors after each functionalization step.

Nanoreactors	**V_{max} (U/mg)**	**K_M (mM)**	**k_{cat} (min^{-1})**
P22-CYP-GOx	0.00681	3.88	187
P22-CYP-GOx-IcG	0.00366	3.50	100

- *Note:* In V_{max}, U represents the enzyme unit, defined as the amount of enzyme that catalyzes the transformation of 1 µmol of substrate per minute.

After the functionalization of IcG, the nanoreactors retained 54% of the original V_{max}, the new Michaelis-Menten constant did not change significantly. This decrease in the maximum velocity is related to the EDC-NHS crosslinking reaction, which can cause the distortion of the GOx enzymes, inactivating them, and affecting the diffusion rate of the substrates. All these factors lead to a change in the kinetic parameters [54,55,89].

P22-CYP-GOx-IcG nanoreactors show combined activity in concentrations of glucose similar to those found in breast cancer cells. Moreover, a high concentration of glucose (>5.5 mM) is usually found in the tumor microenvironment (TME) [56,126,127]. Thus, these nanoreactors are glucose-responsive and can be used to transform CYP-mediated prodrugs into their active metabolites under TME glucose level conditions.

6. Discussion

The present thesis is focused on the design, synthesis, and characterization of smart multimodality nanoplatforms based on P22 virus-like particles with dual therapeutic enzymes and functionalized with indocyanine green. The main objective is to evaluate their potential use in enzyme-prodrug, photodynamic, photothermal, and starvation therapy against breast cancer.

6.1. Enzyme-prodrug and starvation therapies

In 2015, Sánchez-Sánchez et al. reported the synthesis of P22 viral capsids conjugated with CYP_{BM3}21B3 containing the mutation F87A, these new P22-CYP capsids could be activated solely in the presence of H_2O_2 as the final electron acceptor and showed improved stability in acidic pH and protease resistance [44].

In this project, these P22 capsids with CYP_{BM3}21B3 were used due to the high concentration of cytochrome encapsidated and their capacity to transform tamoxifen into its active metabolites. Firstly, the bacterial cell pellets were lysed and then purified with size exclusion column combined to fast protein liquid chromatography (FPLC). After purification, P22-CYP nanoreactors were obtained with 110 CYP molecules inside each capsid, confinement molarity of 3.29 mM, and internal occupancy of 29.9%. The CYP enzyme kinetics were calculated, obtaining a k_{cat} of 1198 min^{-1} and a K_M of 0.36 mM.

Glucose oxidase was subsequently functionalized on P22-CYP nanoreactors to achieve a cascade reaction between glucose oxidase and cytochrome P450 solely in the presence of

glucose. Three different crosslinkage reactions were used to optimize the efficient functionalization to achieve maximum cascade reaction. In all the cases a 1:1 mass ratio of nanoreactors and GOx was used because this was the optimal ratio to achieve the combined enzyme activity according to González-Davis et al. [45].

The three reactions used are reported to form stable conjugates under the performed conditions (pH 7.4, room temperature, aqueous solution). In the first reaction, the amine residues of the proteins will react with glutaraldehyde to form a Schiff base or a Michael type addition [53]. The second reaction is a four-component reaction which implies the use of the amines and carboxylic acids in the protein residues, aldehyde, and isocyanide to form the final α-acetoamido carboxamide derivate, that conjugates the two proteins forming a dipeptide bond [83]. The last reaction was a carbodiimide coupling using EDC and NHS to conjugate amine and carboxylic acids in the residues of the proteins, forming amide covalent bonds [81].

For the first reaction, 0.1% of glutaraldehyde was mixed with GOx and P22-CYP capsids. This reaction did not show combined enzyme activity, possibly because extensive crosslinking with glutaraldehyde caused the distortion of the tertiary GOx structure, obstructing the accessibility of the substrates and affecting the catalytic activity [53,88]. For this reaction, active CYP was in excess compared with active GOx, and the combined activity was possibly limited because the H_2O_2 did not pass the threshold concentration to activate the reaction catalyzed by the cytochrome [45,53].

The second reaction was a four-component reaction proposed by Ugi et al. in 1959 [48]. Formaldehyde and tert-Butyl isocyanide were used in two different compound-enzyme molar ratios, 1:50 and 1:300. These nanoreactors exhibited the highest glucose oxidase activity, which corresponded to a high concentration of GOx functionalized. This increase in the proportion of active GOx compared with active CYP could lead to the inactivation of the

cytochrome due to high concentrations of H_2O_2, which was evident by lower CYP activity in cascade reaction (Figure 27) [45,73].

The last reaction consisted of crosslinking the proteins using carbodiimide chemistry, this reaction showed the highest combined activity of the three reactions, probably because of the optimal ratio of functionalized GOx and CYP in the nanoreactors. Compared with UGI (1:50 molar ratio) nanoreactors, that had the second-highest combined activity, the EDC-NHS nanoreactors had a two-fold higher V_{max} and a better K_{cat} at glucose levels similar to those found in breast cancer cells [56]. For this reason, EDC-NHS nanoreactors were used for the further functionalization of IcG.

The P22-CYP-GOx nanoreactors showed a k_{cat} of 187 min^{-1}. To reach the cascade reaction, the nanoreactors use glucose that is transformed into gluconic acid and H_2O_2 by the GOx, this last compound is later used by the CYP inside the nanoreactors to perform their biocatalytic transformation of substrates.

The normal concentration of glucose in the cells is around 5.5 mM, nevertheless, cancer cells need a large supply of glucose to sustain their growth and proliferation. Tumor microenvironment (TME) usually has high levels of glucose (>5.5 mM) [126,127]. At these glucose concentrations, the nanoreactors showed combined enzyme activity (GOx-CYP), and the cascade reaction can be used to transform CYP-activated prodrugs into their active metabolites (i.e. tamoxifen into endoxifen). Therefore, the nanoreactors are glucose-responsive under glucose levels found in the TME.

The stimuli-responsive nanomaterials are desirable in clinical treatments due to their enhanced selectivity, which diminishes the side effects of conventional therapies [123,124]. This highly localized approach facilitates the development of novel therapies against cancer

(i.e. the systematic toxicity of GOx is reduced when delivery by nanocarriers to cancer cells, therefore, starvation therapy can be achieved) [30,33].

One feasible application of these P22-CYP-GOx nanoreactors is their use in enzyme-prodrug therapy against breast cancer. In this case, the glucose present in breast cancer cells would be converted into gluconic acid, generating H_2O_2 that subsequently will be used by the CYP to transform the prodrug tamoxifen into its active metabolites. This approach is supported by the work of Tapia-Moreno et al., where they used the same P22-CYP viral capsids functionalized with PEG and folic acid, this study reported an increment in the sensitivity of MCF7 cells when simultaneously treated with tamoxifen and P22-CYP capsids. Furthermore, they reported an increase of 4.1 times in the CYP activity after the internalization of the capsids in MCF7 cells [50].

These nanoreactors could also be used for adjuvant starvation and oxidation therapy against breast cancer cells. Glucose oxidase is an enzyme that catalyzes the transformation of glucose using O_2 as the electron acceptor and generating H_2O_2. The following decrease in the concentration of glucose and oxygen leads to a failure in the supply of nutrients and oxygen, decreasing the growth of cancer cells and starving them to death. Moreover, the generation of H_2O_2 increases the oxidative stress in the cells, thus contributing to oxidation therapy [32,74].

6.2. Photodynamic and photothermal therapies

The functionalization of the indocyanine green to the P22-CYP-GOx nanoreactor's surface was performed using EDC and NHS in 1:150 molar ratio, followed by the addition of IcG in the same ratio. This proportion of nanoreactors and IcG was used because higher concentrations of the photosensitizer tend to decrease the combined enzyme activity of the nanoreactors.

After this functionalization, P22-CYP-GOx-IcG nanoreactors retained 54% of the original k_{cat}, being able to transform 100 molecules of substrate per minute per nanoreactor. This reduction in the enzyme activity was expected because EDC-NHS crosslinking used to functionalize IcG can produce the distortion of the GOx, affecting the accessibility of the substrates, and thus modifying the kinetic parameters [54,55,89].

To confirm the functionalization of IcG, the absorbance and fluorescence of the nanoreactors were monitored. P22-CYP-GOx-IcG nanoreactors showed the main absorption peak around 790 nm, and fluorescence between 810-850 nm when excited at 745-760 nm. These absorption and fluorescence behaviors are characteristic of the indocyanine green [57,58]. A calibration curve at 790 nm was used to calculate the amount of IcG functionalized in the nanoreactors, obtaining 10.69 µg/mL, which correspond to 2.84 µg/mg or 101 IcG molecules per nanoreactor.

The generation of ROS under near-infrared light was characterized by a fluorometric ROS assay using a ROS sensitive dye, DPBF and measuring its fluorescence at different exposure times. After 14 minutes under irradiation with a NIR laser (808 nm), only 35% of the original fluorescence was retained. The experiment confirmed the generation of single oxide and superoxide reactive oxygen species due to the excitation of the IcG. This property of the nanoreactors could be used to reach a photodynamic therapy to treat breast cancer cells irradiating them with a NIR source.

The temperature change in a solution of 3.77 mg/mL of P22-CYP-GOx-IcG nanoreactors was monitored under the irradiation of NIR light (808 nm, 0.5 W) for 5 minutes. A maximum change in the temperature was obtained after 280 seconds, with an increase of 3.6°C. *In vitro* studies usually use a temperature of 37°C, therefore, under NIR irradiation it is expected that the nanoreactors would reach a temperature of 40.6°C after 5 minutes.

Theriault et al. reported a cease in the growth of MDA-MB-231 cells exposed at 41°C for 72 hours [69]. Another similar study reported a decrease in cell viability up to 60% in different lines of breast cancer using 40°C for 5 minutes [70]. The P22-CYP-GOx-IcG nanoreactors increased the medium's temperature up to 3.6°C, thus, it is feasible that they could be used for adjuvant photothermal therapy against breast cancer.

P22-CYP-GOx-IcG nanoreactors are NIR light-responsive and are able to generate ROS and increase the temperature of the medium 3.6°C under the irradiation of a NIR laser (0.5 W, 808 nm), thus they can be used in a photodynamic and photothermal therapy for breast cancer.

6.3. Combination therapy

The next diagram briefly describes the mechanisms that the nanoreactors undergo to reach the different therapies proposed in this thesis, the software UCSF Chimera 1.14 was used to simulate the nanoreactors (Figure 30).

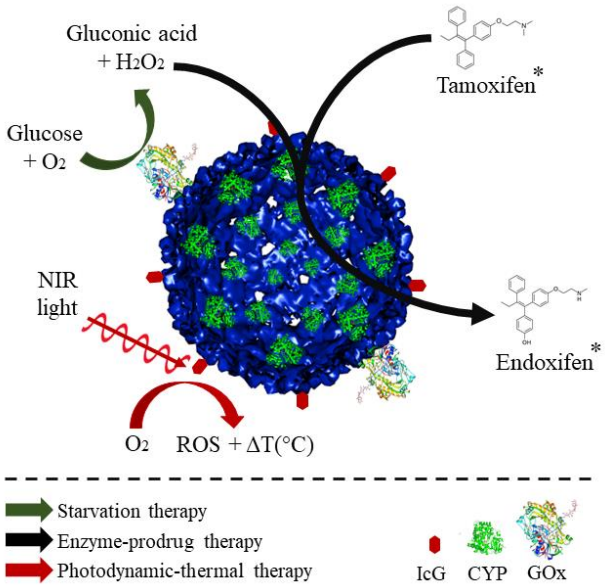

Figure 30. Schematic representation of the processes that take place in the P22-CYP-GOx-IcG nanoreactors to achieve a combination therapy. *In the present study the transformation of DMP was monitored instead of tamoxifen, but this is the proposed mechanism that tamoxifen would undergo in the enzyme cascade.

The final P22-CYP-GOx-IcG nanoreactors are suitable for their use in a combination enzyme-prodrug, starvation, photodynamic, and photothermal therapies against breast cancer. These nanoreactors can use glucose concentrations in the order of 10^{-6} mol/L as a substrate to start a cascade reaction between GOx and CYP, showing a combined k_{cat} of 100 min^{-1}. In addition, under NIR irradiation the nanoreactors are capable to generate ROS and increase the solution's temperature up to 3.6°C with the laser power as low as 0.5 W.

P22-CYP-GOx-IcG nanoreactors showed combined activity at glucose concentrations that are normally found in breast cancer cells [56], therefore, the GOx-CYP cascade reaction could be used to transform tamoxifen into its active metabolites inside breast cancer cells. In this process, GOx would cause a decrease in the concentration of O_2 and glucose, which could lead to cell deprivation of nutrients and oxygen. Moreover, the irradiation of NIR light would likely generate oxidative stress and hyperthermia in cancer cells.

7. Conclusions

P22 viral capsids with CYP activity were purified by fast protein liquid chromatography, obtaining 110 CYP molecules inside each capsid. The P22-CYP nanoreactors were able to transform 1198 molecules of substrate (DMP) per capsid per minute.

The use of EDC and NHS in 1:200 molar ratio was the best strategy amongst the tested reactions to functionalize glucose oxidase to the P22-CYP nanoreactors achieving the highest turnover number for GOx-CYP combined activity. The combined k_{cat} of the P22-CYP-GOx nanoreactors was 187 min^{-1}, which decreased to 100 min^{-1} after the functionalization of indocyanine green.

The functionalization of IcG was performed with the use of EDC and NHS in 1:150 molar ratio, obtaining a concentration of 2.84 µg of IcG per mg of nanoreactors, equivalent to 101 IcG functionalized molecules per nanoreactor. P22-CYP-GOx-IcG nanoreactors showed the generation of ROS and the increase in temperature up to 3.6°C under NIR irradiation (808 nm).

After the functionalization of each compound, the nanoreactors incremented their hydrodynamic diameter without a significant change in their zeta potential. TEM micrographs showed the characteristic icosahedral structure of the P22 capsids with an average diameter of 58.8 nm.

Overall, P22-CYP-GOx-IcG nanoreactors were successfully synthesized and characterized, showing a potential use as multimodal nanoplatforms for quadruple combination therapy against breast cancer.

8. Perspectives

Future work includes the use of tamoxifen to corroborate its transformation to endoxifen and other active metabolites by the cascade reaction of GOx and CYP. Cytotoxic assays are necessary to evaluate the decrease of cell viability in breast cancer cells using the proposed nanoreactors. These assays would be performed under different conditions, such as the addition of tamoxifen in the solution, the irradiation of near-infrared light, and the use of different concentrations of the nanoreactors. Cellular assays would be useful to corroborate if the nanoreactors have the predicted behaviors described in this thesis for *in vitro* studies and to evaluate their potential use for *in vivo* studies.

Another approach consists of the synthesis of a tamoxifen derivate containing a thiol group, this derivate would be conjugated with polyethylene glycol and functionalized to the nanoreactors for the controlled release of the prodrug under a reducing environment. These nanoreactors would be completely self-sufficient to reach a combination therapy without the previous administration of tamoxifen to the cancer cells.

Note: *Experimental work to functionalize tamoxifen on the surface of the nanoreactors was started. More information can be found in Appendix I of this thesis.*

Appendix I: Tamoxifen functionalization approach

Note: *Due to the health emergency declared by the Mexican government in the context of the COVID-19 pandemic, this part of the experimental section remained incomplete. This appendix shows the main results obtained and the following steps.*

One of the original objectives was the functionalization of tamoxifen on the surface of the nanoreactors. This approach consisted of multiple reactions for the transformation of tamoxifen into a tamoxifen derivate containing a thiol group (TAM-SH), then the nanoreactors would react with the compound OPSS-PEG-NHS (Sigma Aldrich) to obtain P22-CYP-GOx-IcG-PEG-OPSS nanoreactors, these would subsequently react with TAM-SH to obtain pegylated nanoreactors functionalized with tamoxifen linked by a disulfide bond. This S-S bond could finally be break into reducing environments, delivering the tamoxifen to the medium (Figure 31).

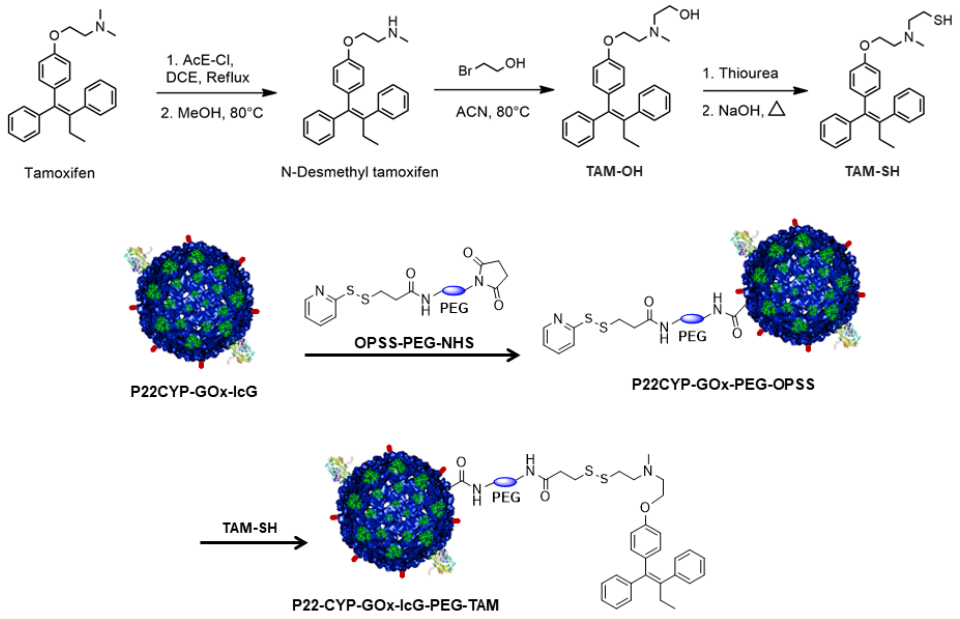

Figure 31. Schematic representation of the different steps to obtain pegylated nanoreactors functionalized with a tamoxifen derivate using disulfide bonds. These nanoreactors would be self-sufficient to reach a combination therapy against breast cancer without the previous administration of tamoxifen.

In the present thesis, the transformation of tamoxifen into a derivate containing a hydroxy group (TAM-OH) was performed according to the protocol described by Dreaden et al. in 2009 [122]. To characterize this compound, 1 ng of was injected into the LC-MS (liquid chromatography-mass spectrometry) equipment (Figure 32).

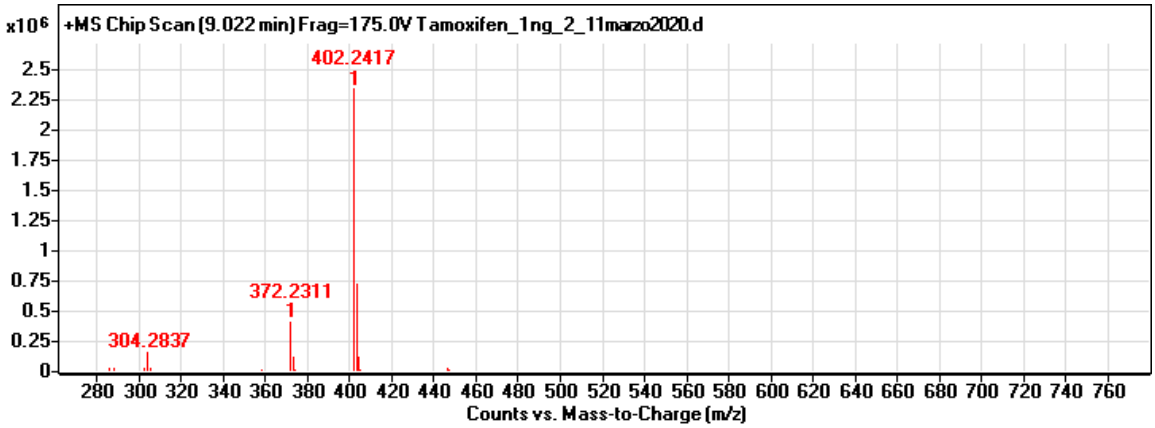

Figure 32. High resolution mass spectroscopy of TAM-OH. The peak in 402.24 m/z corresponds to TAM-OH, with a theoretical molecular weight of 402.52 g/mol.

A strong signal (range 1x106) of a peak 402.2417 m/z with a mass error of 3.9 ppm was obtained. Compared to the theoretical mass of the molecule of interest (402.52 g/mol), it could be corroborated the generation of TAM-OH. The transformation of TAM-OH into TAM-SH, the functionalization of OPSS-PEG-NHS on the nanoreactors, and the final reaction with TAM-SH remain to be done.

Bibliography

[1]. Torre, L. A., Siegel, R. L., Ward, E. M., & Jemal, A. (2016). Global cancer incidence and mortality rates and trends—an update. Cancer Epidemiology and Prevention Biomarkers, 25(1), 16-27.

[2]. American Cancer Society. (2010). The global economic cost of cancer. Obtained from the website of the ACS.

[3]. Anand, P., Kunnumakara, A. B., Sundaram, C., Harikumar, K. B., Tharakan, S. T., Lai, O. S., & Aggarwal, B. B. (2008). Cancer is a preventable disease that requires major lifestyle changes. Pharmaceutical Research, 25(9), 2097-2116.

[4]. Vogelstein, B., & Kinzler, K. W. (1993). The multistep nature of cancer. Trends in Genetics, 9(4), 138-141.

[5]. Vos, T., Abajobir, A. A., Abate, K. H., Abbafati, C., Abbas, K. M., Abd-Allah, F., & Aboyans, V. (2017). Global, regional, and national incidence, prevalence, and years lived with disability for 328 diseases and injuries for 195 countries, 1990–2016: a systematic analysis for the Global Burden of Disease Study 2016. The Lancet, 390(10100), 1211-1259.

[6]. Bray, F., Ferlay, J., Soerjomataram, I., Siegel, R. L., Torre, L. A., & Jemal, A. (2018). Global cancer statistics 2018: GLOBOCAN estimates of incidence and mortality worldwide for 36 cancers in 185 countries. CA: A Cancer Journal for Clinicians, 68(6), 394-424.

[7]. Feng, Y., Spezia, M., Huang, S., Yuan, C., Zeng, Z., Zhang, L., & Liu, B. (2018). Breast cancer development and progression: Risk factors, cancer stem cells, signaling pathways, genomics, and molecular pathogenesis. Genes & Diseases, 5(2), 77-106.

[8]. Sharma, G. N., Dave, R., Sanadya, J., Sharma, P., & Sharma, K. K. (2010). Various types and management of breast cancer: an overview. Journal of Advanced Pharmaceutical Technology & Research, 1(2), 109.

[9]. Waks, A. G., & Winer, E. P. (2019). Breast cancer treatment: a review. Jama, 321(3), 288-300.

[10]. Mukerabigwi, J. F., Ge, Z., & Kataoka, K. (2018). Therapeutic nanoreactors as in vivo nanoplatforms for cancer therapy. Chemistry–A European Journal, 24(59), 15706-15724.

[11]. Li, J., Li, Y., Wang, Y., Ke, W., Chen, W., Wang, W., & Ge, Z. (2017). Polymer prodrug-based nanoreactors activated by tumor acidity for orchestrated oxidation/chemotherapyy. Nano Letters, 17(11), 6983-6990.

[12]. Yu, Z., Zhou, P., Pan, W., Li, N., & Tang, B. (2018). A biomimetic nanoreactor for synergistic chemiexcited photodynamic therapy and starvation therapy against tumor metastasis. Nature Communications, 9(1), 1-9.

[13]. Baumann, P., Spulber, M., Dinu, I. A., & Palivan, C. G. (2014). Cellular trojan horse based polymer nanoreactors with light-sensitive activity. The Journal of Physical Chemistry B, 118(31), 9361-9370.

[14]. Huo, M., Wang, L., Chen, Y., & Shi, J. (2017). Tumor-selective catalytic nanomedicine by nanocatalyst delivery. Nature Communications, 8(1), 1-12.

[15]. Miller, M. A., Askevold, B., Mikula, H., Kohler, R. H., Pirovich, D., & Weissleder, R. (2017). Nano-palladium is a cellular catalyst for in vivo chemistry. Nature Communications, 8(1), 1-13.

[16]. Gama, P. (2019). Nanobiorreactores con actividad enzimática como terapia para la galactosemia clásica (Tesis de maestría en ciencias). Centro de Investigación Científica y de Educación Superior de Ensenada, Baja California.

[17]. Wen A.M., Lee K.L., Steinmetz N.F. (2020) Plant Virus-Based Nanotechnologies. In: Norris P., Friedersdorf L. (eds) Women in Nanotechnology. Women in Engineering and Science. Springer, Cham.

[18]. Ma, Y., Nolte, R. J., & Cornelissen, J. J. (2012). Virus-based nanocarriers for drug delivery. Advanced Drug Delivery Reviews, 64(9), 811-825.

[19]. Schoonen, L., & van Hest, J. C. (2014). Functionalization of protein-based nanocages for drug delivery applications. Nanoscale, 6(13), 7124-7141.

[20]. Patterson, D. P., Prevelige, P. E., & Douglas, T. (2012). Nanoreactors by programmed enzyme encapsulation inside the capsid of the bacteriophage P22. ACS Nano, 6(6), 5000-5009.

[21]. Parent, K. N., Khayat, R., Tu, L. H., Suhanovsky, M. M., Cortines, J. R., Teschke, C. M., ... & Baker, T. S. (2010). P22 coat protein structures reveal a novel mechanism for capsid maturation: stability without auxiliary proteins or chemical crosslinks. Structure, 18(3), 390-401.

[22]. Wu, Y., Yang, H., & Shin, H. J. (2013). Viruses as self-assembled nanocontainers for encapsulation of functional cargoes. Korean Journal of Chemical Engineering, 30(7), 1359-1367.

[23]. Xu, G., & McLeod, H. L. (2001). Strategies for enzyme/prodrug cancer therapy. Clinical Cancer Research, 7(11), 3314-3324.

[24]. Clemons, M., Danson, S., & Howell, A. (2002). Tamoxifen ('Nolvadex'): a review: Antitumour treatment. Cancer Treatment Reviews, 28(4), 165-180.

[25]. Osborne, C. K. (1998). Tamoxifen in the treatment of breast cancer. New England Journal of Medicine, 339(22), 1609-1618.

[26]. Pearce, S. T., & Jordan, V. C. (2004). The biological role of estrogen receptors α and β in cancer. Critical Reviews in Oncology/Hematology, 50(1), 3-22.

[27]. Danielson, P. Á. (2002). The cytochrome P450 superfamily: biochemistry, evolution and drug metabolism in humans. Current Drug Metabolism, 3(6), 561-597.

[28]. Cirino, P. C., & Arnold, F. H. (2003). A self-sufficient peroxide-driven hydroxylation biocatalyst. Angewandte Chemie International Edition, 42(28), 3299-3301.

[29]. Sanchez-Sanchez, L., Roman, R., & Vazquez-Duhalt, R. (2012). Pesticide transformation by a variant of CYPBM3 with improved peroxygenase activity. Pesticide Biochemistry and Physiology, 102(2), 169-174.

[30]. Zhang, R., Feng, L., Dong, Z., Wang, L., Liang, C., Chen, J., ... & Liu, Z. (2018). Glucose & oxygen exhausting liposomes for combined cancer starvation and hypoxia-activated therapy. Biomaterials, 162, 123-131.

[31]. Dinda, S., Sarkar, S., & Das, P. K. (2018). Glucose oxidase mediated targeted cancer-starving therapy by biotinylated self-assembled vesicles. Chemical Communications, 54(71), 9929-9932.

[32]. Fu, L. H., Qi, C., Lin, J., & Huang, P. (2018). Catalytic chemistry of glucose oxidase in cancer diagnosis and treatment. Chemical Society Reviews, 47(17), 6454-6472.

[33]. Zhao, W., Hu, J., & Gao, W. (2017). Glucose oxidase–polymer nanogels for synergistic cancer-starving and oxidation therapy. ACS Applied Materials & Interfaces, 9(28), 23528-23535.

[34]. Dolmans, D. E., Fukumura, D., & Jain, R. K. (2003). Photodynamic therapy for cancer. Nature Reviews Cancer, 3(5), 380-387.

[35]. Agostinis, P., Berg, K., Cengel, K. A., Foster, T. H., Girotti, A. W., Gollnick, S. O., ... & Korbelik, M. (2011). Photodynamic therapy of cancer: an update. CA: A Cancer Journal for Clinicians, 61(4), 250-281.

[36]. Shibu, E. S., Hamada, M., Murase, N., & Biju, V. (2013). Nanomaterials formulations for photothermal and photodynamic therapy of cancer. Journal of Photochemistry and Photobiology C: Photochemistry Reviews, 15, 53-72.

[37]. Chen, M., Fang, X., Tang, S., & Zheng, N. (2012). Polypyrrole nanoparticles for high-performance in vivo near-infrared photothermal cancer therapy. Chemical Communications, 48(71), 8934-8936.

[38]. Shirata, C., Kaneko, J., Inagaki, Y., Kokudo, T., Sato, M., Kiritani, S., ... & Kokudo, N. (2017). Near-infrared photothermal/photodynamic therapy with indocyanine green induces apoptosis of hepatocellular carcinoma cells through oxidative stress. Scientific Reports, 7(1), 1-8.

[39]. Tamai, K., Mizushima, T., Wu, X., Inoue, A., Ota, M., Yokoyama, Y., ... & Hata, T. (2018). Photodynamic therapy using indocyanine green loaded on super carbonate apatite as minimally invasive cancer treatment. Molecular Cancer Therapeutics, 17(7), 1613-1622.

[40]. Alander, J. T., Kaartinen, I., Laakso, A., Pätilä, T., Spillmann, T., Tuchin, V. V., ... & Välisuo, P. (2012). A review of indocyanine green fluorescent imaging in surgery. International Journal of Biomedical Imaging, 2012

[41]. Yuan, B., Chen, N., & Zhu, Q. (2004). Emission and absorption properties of indocyanine green in Intralipid solution. Journal of Biomedical Optics, 9(3), 497-504.

[42]. Chen, Y., Li, H., Deng, Y., Sun, H., Ke, X., & Ci, T. (2017). Near-infrared light triggered drug delivery system for higher efficacy of combined chemo-photothermal treatment. Acta Biomaterialia, 51, 374-392.

[43]. Liu, B., Li, C., Chen, G., Liu, B., Deng, X., Wei, Y., ... & Lin, J. (2017). Synthesis and optimization of MoS2@ Fe3O4-ICG/Pt (IV) nanoflowers for MR/IR/PA bioimaging and combined PTT/PDT/chemotherapy triggered by 808 nm laser. Advanced Science, 4(8), 1600540.

[44]. Sánchez-Sánchez, L., Tapia-Moreno, A., Juarez-Moreno, K., Patterson, D. P., Cadena-Nava, R. D., Douglas, T., & Vazquez-Duhalt, R. (2015). Design of a VLP-nanovehicle for CYP450 enzymatic activity delivery. Journal of Nanobiotechnology, 13(1), 66.

[45]. González-Davis, O., Chauhan, K., Zapian-Merino, S. J., & Vazquez-Duhalt, R. (2020). Bi-enzymatic virus-like bionanoreactors for the transformation of endocrine disruptor compounds. International Journal of Biological Macromolecules.

[46]. Chauhan, K., Hernandez-Meza, J. M., Rodriguez-Hernandez, A. G., Juarez-Moreno, K., Sengar, P., & Vazquez-Duhalt, R. (2018). Multifunctionalized biocatalytic P22 nanoreactor for combinatory treatment of ER+ breast cancer. Journal of Nanobiotechnology, 16(1), 17.

[47]. Tafoya, P. (2017). Diseño de nanopartículas virales con actividad citocromo P450 con NADPH como fuente de electrones (Maestría en ciencias). Centro de Investigación Científica y de Educación Superior de Ensenada, Baja California.

[48]. Ugi, I., Meyr, R., & Steinbruckner, C. (1959). Versammlungsberichte. Angew Chem, 71, 373-388.

[49]. Tayefi-Nasrabadi, H., Dehghan, G., Daeihassani, B., Movafegi, A., & Samadi, A. (2011). Some biochemical properties of guaiacol peroxidases as modified by salt stress in leaves of salt-tolerant and salt-sensitive safflower (Carthamus tinctorius L. cv.) cultivars. African Journal of Biotechnology, 10(5), 751-763.

[50]. Tapia-Moreno, A., Juarez-Moreno, K., Gonzalez-Davis, O., Cadena-Nava, R. D., & Vazquez-Duhalt, R. (2017). Biocatalytic virus capsid as nanovehicle for enzymatic activation of Tamoxifen in tumor cells. Biotechnology Journal, 12(6), 1600706.

[51]. Tapia, M. (2015). Funcionalización y direccionamiento de partículas tipo virus del bacteriófago P22 con actividad citocromo P450 (Maestrías en ciencias). Centro de Investigación Científica y de Educación Superior de Ensenada, Baja California.

[52]. Zlotnick, A., Suhanovsky, M. M., & Teschke, C. M. (2012). The energetic contributions of scaffolding and coat proteins to the assembly of bacteriophage procapsids. Virology, 428(1), 64-69.

[53]. Migneault, I., Dartiguenave, C., Bertrand, M. J., & Waldron, K. C. (2004). Glutaraldehyde: behavior in aqueous solution, reaction with proteins, and application to enzyme crosslinking. Biotechniques, 37(5), 790-802.

[54]. Comellas-Aragonès, M., Engelkamp, H., Claessen, V. I., Sommerdijk, N. A., Rowan, A. E., Christianen, P. C., ... & Nolte, R. J. (2007). A virus-based single-enzyme nanoreactor. Nature Nanotechnology, 2(10), 635.

[55]. Norris, M. G., & Malys, N. (2011). What is the true enzyme kinetics in the biological system? An investigation of macromolecular crowding effect upon enzyme kinetics of glucose-6-phosphate dehydrogenase. Biochemical and Biophysical Research Communications, 405(3), 388-392.

[56]. Nascimento, R. A., Özel, R. E., Mak, W. H., Mulato, M., Singaram, B., & Pourmand, N. (2016). Single cell “glucose nanosensor” verifies elevated glucose levels in individual cancer cells. Nano Letters, 16(2), 1194-1200.

[57]. Landsman, M. L., Kwant, G., Mook, G. A., & Zijlstra, W. G. (1976). Light-absorbing properties, stability, and spectral stabilization of indocyanine green. Journal of Applied Physiology, 40(4), 575-583.

[58]. Gathje, J., Steuer, R. R., & Nicholes, K. R. (1970). Stability studies on indocyanine green dye. Journal of Applied Physiology, 29(2), 181-185.

[59]. Shemesh, C. S., Hardy, C. W., David, S. Y., Fernandez, B., & Zhang, H. (2014). Indocyanine green loaded liposome nanocarriers for photodynamic therapy using human triple negative breast cancer cells. Photodiagnosis and Photodynamic Therapy, 11(2), 193-203.

[60]. Wozniak, M., Tanfani, F., Bertoli, E., Zolese, G., & Antosiewicz, J. (1991). A new fluorescence method to detect singlet oxygen inside phospholipid model membranes. Biochimica et Biophysica Acta (BBA)-Lipids and Lipid Metabolism, 1082(1), 94-100.

[61]. Ohyashiki, T., Nunomura, M., & Katoh, T. (1999). Detection of superoxide anion radical in phospholipid liposomal membrane by fluorescence quenching method using 1, 3-diphenylisobenzofuran. Biochimica et Biophysica Acta (BBA)-Biomembranes, 1421(1), 131-139.

[62]. Wang, X. H., Yu, Y. X., Cheng, K., Yang, W., Liu, Y. A., & Peng, H. S. (2019). Polylysine modified conjugated polymer nanoparticles loaded with the singlet oxygen probe 1, 3-diphenylisobenzofuran and the photosensitizer indocyanine green for use in fluorometric sensing and in photodynamic therapy. Microchimica Acta, 186(12), 842.

[63]. Huang, S., Fong, C. I., Xu, M., Han, B. N., Yuan, Z., & Zhao, Q. (2019). Nano-loaded natural killer cells as carriers of indocyanine green for synergetic cancer immunotherapy and phototherapy. Journal of Innovative Optical Health Sciences, 12(03), 1941002.

[64]. Shan, W., Chen, R., Zhang, Q., Zhao, J., Chen, B., Zhou, X., ... & Ren, L. (2018). Improved Stable Indocyanine Green (ICG)-Mediated Cancer Optotheranostics with Naturalized Hepatitis B Core Particles. Advanced Materials, 30(28), 1707567.

[65]. Wan, Z., Mao, H., Guo, M., Li, Y., Zhu, A., Yang, H., ... & Ge, C. (2014). Highly efficient hierarchical micelles integrating photothermal therapy and singlet oxygen-synergized chemotherapy for cancer eradication. Theranostics, 4(4), 399.

[66]. Long, S., Xu, Y., Zhou, F., Wang, B., Yang, Y., Fu, Y., ... & Li, X. (2019). Characteristics of temperature changes in photothermal therapy induced by combined application of indocyanine green and laser. Oncology Letters, 17(4), 3952-3959.

[67]. Januszewski, A., & Stebbing, J. (2014). Hyperthermia in cancer: is it coming of age?. Lancet Oncology, 15(6), 565.

[68]. Wust, P., Hildebrandt, B., Sreenivasa, G., Rau, B., Gellermann, J., Riess, H., ... & Schlag, P. M. (2002). Hyperthermia in combined treatment of cancer. The Lancet Oncology, 3(8), 487-497.

[69]. Theriault, C., Paetzell, E., Chandrasekar, R., Barkey, C., Oni, Y., & Soboyejo, W. O. (2012). An in-vitro study of the effects of temperature on breast cancer cells: Experiments and models. Materials Science and Engineering: C, 32(8), 2242-2249.

[70]. Thompson, E. A., Graham, E., MacNeill, C. M., Young, M., Donati, G., Wailes, E. M., ... & Levi-Polyachenko, N. H. (2014). Differential response of MCF7, MDA-MB-231, and MCF 10A cells to hyperthermia, silver nanoparticles and silver nanoparticle-induced photothermal therapy. International Journal of Hyperthermia, 30(5), 312-323.

[71]. Earnshaw, W., Casjens, S., & Harrison, S. C. (1976). Assembly of the head of bacteriophage P22: x-ray diffraction from heads, proheads and related structures. Journal of Molecular Biology, 104(2), 387-410.

[72]. Shenoy, R., & Bowman, C. N. (2012). Kinetics of interfacial radical polymerization initiated by a glucose-oxidase mediated redox system. Biomaterials, 33(29), 6909-6914.

[73]. Valderrama, B., Ayala, M., & Vazquez-Duhalt, R. (2002). Suicide inactivation of peroxidases and the challenge of engineering more robust enzymes. Chemistry & Biology, 9(5), 555-565.

[74]. Yu, J., Qian, C., Zhang, Y., Cui, Z., Zhu, Y., Shen, Q., ... & Gu, Z. (2017). Hypoxia and H2O2 dual-sensitive vesicles for enhanced glucose-responsive insulin delivery. Nano Letters, 17(2), 733-739.

[75]. Zeng, J., Sauter, E. R., & Li, B. (2020). FABP4: A New Player in Obesity-Associated Breast Cancer. Trends in Molecular Medicine, 26(5), 437-440.

[76]. Calixto, G. M. F., Bernegossi, J., De Freitas, L. M., Fontana, C. R., & Chorilli, M. (2016). Nanotechnology-based drug delivery systems for photodynamic therapy of cancer: a review. Molecules, 21(3), 342.

[77]. Szablewski, L. (2013). Expression of glucose transporters in cancers. Biochimica et Biophysica Acta (BBA)-Reviews on Cancer, 1835(2), 164-169.

[78]. Kapoor, M. (1996). How to cross-link proteins. Cellular, Molecular and Microbial Biology Division, University of Calgary, Calgary, Canada, T2N 1N4.

[79]. Quiocho, F. A., & Richards, F. M. (1964). Intermolecular cross linking of a protein in the crystalline state: carboxypeptidase-A. Proceedings of the National Academy of Sciences of the United States of America, 52(3), 833.

[80]. Peters, K., & Richards, F. M. (1977). Chemical cross-linking: reagents and problems in studies of membrane structure. Annual Review of Biochemistry, 46(1), 523-551.

[81]. Hermanson, G. (2013). Bioconjugate techniques (pp. 259-273). Academic Press.

[82]. Thermo Scientific. Crosslinking Technical Handbook. Obtained from: tools.thermofisher.com/content/sfs/brochures/1602163-Crosslinking-Reagents-Handbook.pdf

[83]. Rocha, R. O., Rodrigues, M. O., & Neto, B. A. (2020). Review on the Ugi Multicomponent Reaction Mechanism and the Use of Fluorescent Derivatives as Functional Chromophores. ACS Omega, 5(2), 972–979.

[84]. Pérez-Labrada, K., Brouard, I., Méndez, I., & Rivera, D. G. (2012). Multicomponent synthesis of Ugi-type ceramide analogues and neoglycolipids from lipidic isocyanides. The Journal of Organic Chemistry, 77(10), 4660-4670.

[85]. Arabanian, A., Mohammadnejad, M., Balalaie, S., & Gross, J. H. (2009). Synthesis of novel Gn-RH analogues using Ugi-4MCR. Bioorganic & Medicinal Chemistry Letters, 19(3), 887-890.

[86]. Morales, F. E., Garay, H. E., Muñoz, D. F., Augusto, Y. E., Otero-González, A. J., Reyes Acosta, O., & Rivera, D. G. (2015). Aminocatalysis-mediated on-resin Ugi reactions: application in the solid-phase synthesis of N-substituted and tetrazolo lipopeptides and peptidosteroids. Organic Letters, 17(11), 2728-2731.

[87]. Marek, M., Jarý, J., Valentova, O., & Vodrážka, Z. (1983). Immobilization of glycoenzymes by means of their glycosidic components. Biotechnology Letters, 5(10), 653-658.

[88]. Rojas, M. J., Amaral-Fonseca, M., Zanin, G. M., Fernandez-Lafuente, R., Giordano, R. D. L. C., & Tardioli, P. W. (2019). Preparation of crosslinked enzyme aggregates of a thermostable cyclodextrin glucosyltransferase from Thermoanaerobacter sp. Critical effect of the crosslinking agent. Catalysts, 9(2), 120.

[89]. Lazar, T. (2005). Susan R. Mikkelsen, Eduardo Corton: Bioanalytical Chemistry. Analytical and Bioanalytical Chemistry, 383(7-8), 1030-1031.

[90]. Marangoni, A. G. (2003). Enzyme kinetics: a modern approach. John Wiley & Sons.

[91]. Berg, J., Tymoczko, J., & Stryer, L. (2012). Biochemistry. Freeman.

[92]. Nagar, S., Argikar, U., & Tweedie, D. (2014). Enzyme Kinetics in Drug Metabolism: Fundamentals and Applications. Humana Press.

[93]. Leduc, P. R., Wong, M. S., Ferreira, P. M., Groff, R. E., Haslinger, K., Koonce, M. P., ... & Rotello, V. M. (2007). Towards an in vivo biologically inspired nanofactory. Nature Nanotechnology, 2(1), 3-7.

[94]. Nishimura, T., & Akiyoshi, K. (2018). Biotransporting Biocatalytic Reactors toward Therapeutic Nanofactories. Advanced Science, 5(11), 1800801.

[95]. Sibata, C. H., Colussi, V. C., Oleinick, N. L., & Kinsella, T. J. (2000). Photodynamic therapy: a new concept in medical treatment. Brazilian Journal of Medical and Biological Research, 33, 869-880.

[96]. Karotki, A., Kruk, M., Drobizhev, M., Rebane, A., Nickel, E., & Spangler, C. W. (2001). Efficient singlet oxygen generation upon two-photon excitation of new porphyrin with enhanced nonlinear absorption. IEEE Journal of Selected Topics in Quantum Electronics, 7(6), 971-975.

[97]. Juzeniene, A., Nielsen, K. P., & Moan, J. (2006). Biophysical aspects of photodynamic therapy. Journal of Environmental Pathology, Toxicology and Oncology, 25(1-2).

[98]. Plaetzer, K., Krammer, B., Berlanda, J., Berr, F., & Kiesslich, T. (2009). Photophysics and photochemistry of photodynamic therapy: fundamental aspects. Lasers in Medical Science, 24(2), 259-268.

[99]. Lyons, S. K., Patrick, P. S., & Brindle, K. M. (2013). Imaging mouse cancer models in vivo using reporter transgenes. Cold Spring Harbor Protocols, 2013(8).

[100]. Ruggiero, E., Alonso-de Castro, S., Habtemariam, A., & Salassa, L. (2016). Upconverting nanoparticles for the near infrared photoactivation of transition metal complexes: new opportunities and challenges in medicinal inorganic photochemistry. Dalton Transactions, 45(33), 13012-13020.

[101]. Wang, J., Liu, G., Cham-Fai Leung, K., Loffroy, R., Lu, P. X., & Wang, X. J. (2015). Opportunities and challenges of fluorescent carbon dots in translational optical imaging. Current Pharmaceutical Design, 21(37), 5401-5416.

[102]. Koyani, R. D., & Vazquez-Duhalt, R. (2018). Enzymatic activation of the emerging drug resveratrol. Applied Biochemistry and Biotechnology, 185(1), 248-256.

[103]. Patterson, D. P., Schwarz, B., El-Boubbou, K., van der Oost, J., Prevelige, P. E., & Douglas, T. (2012). Virus-like particle nanoreactors: programmed encapsulation of the thermostable CelB glycosidase inside the P22 capsid. Soft Matter, 8(39), 10158-10166.

[104]. Patterson, D. P., Schwarz, B., Waters, R. S., Gedeon, T., & Douglas, T. (2013). Encapsulation of an enzyme cascade within the bacteriophage P22 virus-like particle. ACS Chemical Biology, 9(2), 359-365.

[105]. Fujita, K. I. (2006). Cytochrome P450 and anticancer drugs. Current Drug Metabolism, 7(1), 23-37.

[106]. August, J. T., Murad, F., Anders, M. W., Coyle, J. T., & Li, A. P. (1997). Drug-Drug interactions: scientific and regulatory perspectives. Academic Press.

[107]. Goetz, M. P., Kamal, A., & Ames, M. M. (2008). Tamoxifen pharmacogenomics: the role of CYP2D6 as a predictor of drug response. Clinical Pharmacology & Therapeutics, 83(1), 160-166.

[108]. El-Rayes, B. F., Ali, S., Heilbrun, L. K., Lababidi, S., Bouwman, D., Visscher, D., & Philip, P. A. (2003). Cytochrome p450 and glutathione transferase expression in human breast cancer. Clinical Cancer Research, 9(5), 1705-1709.

[109]. Murray, G. I., Patimalla, S., Stewart, K. N., Miller, I. D., & Heys, S. D. (2010). Profiling the expression of cytochrome P450 in breast cancer. Histopathology, 57(2), 202-211.

[110]. Vaclavikova, R., Hubackova, M., Stribrna-Sarmanova, J., Kodet, R., Mrhalova, M., Novotny, J. A. N., ... & Soucek, P. (2007). RNA expression of cytochrome P450 in breast cancer patients. Anticancer Research, 27(6C), 4443-4450.

[111]. Chiocca, E. A., & Waxman, D. J. (2004). Cytochrome P450-based gene therapies for cancer. In Suicide Gene Therapy (pp. 203-222). Humana Press.

[112]. Doughty, A. C., Hoover, A. R., Layton, E., Murray, C. K., Howard, E. W., & Chen, W. R. (2019). Nanomaterial applications in photothermal therapy for cancer. Materials, 12(5), 779.

[113]. Hildebrandt, B., Wust, P., Ahlers, O., Dieing, A., Sreenivasa, G., Kerner, T., ... & Riess, H. (2002). The cellular and molecular basis of hyperthermia. Critical Reviews in Oncology/Hematology, 43(1), 33-56.

[114]. Niidome, T., Yamagata, M., Okamoto, Y., Akiyama, Y., Takahashi, H., Kawano, T., ... & Niidome, Y. (2006). PEG-modified gold nanorods with a stealth character for in vivo applications. Journal of Controlled Release, 114(3), 343-347.

[115]. Yang, K., Zhang, S., Zhang, G., Sun, X., Lee, S. T., & Liu, Z. (2010). Graphene in mice: ultrahigh in vivo tumor uptake and efficient photothermal therapy. Nano Letters, 10(9), 3318-3323.

[116]. Zhou, F., Da, X., Ou, Z., Wu, B., Resasco, D. E., & Chen, W. R. (2009). Cancer photothermal therapy in the near-infrared region by using single-walled carbon nanotubes. Journal of Biomedical Optics, 14(2), 021009.

[117]. Chen, Q., Xu, L., Liang, C., Wang, C., Peng, R., & Liu, Z. (2016). Photothermal therapy with immune-adjuvant nanoparticles together with checkpoint blockade for effective cancer immunotherapy. Nature Communications, 7(1), 1-13.

[118]. Jin, Y., Yang, X., & Tian, J. (2018). Targeted polypyrrole nanoparticles for the identification and treatment of hepatocellular carcinoma. Nanoscale, 10(20), 9594-9601.

[119]. Tian, B., Wang, C., Zhang, S., Feng, L., & Liu, Z. (2011). Photothermally enhanced photodynamic therapy delivered by nano-graphene oxide. ACS Nano, 5(9), 7000-7009.

[120]. Altınogˇlu, E. I., Russin, T. J., Kaiser, J. M., Barth, B. M., Eklund, P. C., Kester, M., & Adair, J. H. (2008). Near-infrared emitting fluorophore-doped calcium phosphate nanoparticles for in vivo imaging of human breast cancer. ACS Nano, 2(10), 2075-2084.

[121]. Li, Z., Yin, Q., Chen, B., Wang, Z., Yan, Y., Qi, T., ... & Wang, Y. (2019). Ultra-pH-sensitive indocyanine green-conjugated nanoprobes for fluorescence imaging-guided photothermal cancer therapy. Nanomedicine: Nanotechnology, Biology and Medicine, 17, 287-296.

[122]. Dreaden, E. C., Mwakwari, S. C., Sodji, Q. H., Oyelere, A. K., & El-Sayed, M. A. (2009). Tamoxifen− poly (ethylene glycol)− thiol gold nanoparticle conjugates: enhanced potency and selective delivery for breast cancer treatment. Bioconjugate Chemistry, 20(12), 2247-2253.

[123]. Zhang, Y., Li, M., Gao, X., Chen, Y., & Liu, T. (2019). Nanotechnology in cancer diagnosis: progress, challenges and opportunities. Journal of Hematology & Oncology, 12(1), 137.

[124]. Li, X., Zhang, C., Le Guyader, L., & Chen, C. (2010). “Smart” nanomaterials for cancer therapy. Science China Chemistry, 53(11), 2241-2249.

[125]. Van der Meel, R., Sulheim, E., Shi, Y., Kiessling, F., Mulder, W., & Lammers, T. (2019). Nature Nanotechnology, 14, 1007-1017.

[126]. Li, W., Zhang, X., Sang, H., Zhou, Y., Shang, C., Wang, Y., & Zhu, H. (2019). Effects of hyperglycemia on the progression of tumor diseases. Journal of Experimental & Clinical Cancer Research, 38(1), 327.

[127]. Duan, W., Shen, X., Lei, J., Xu, Q., Yu, Y., Li, R., ... & Ma, Q. (2014). Hyperglycemia, a neglected factor during cancer progression. BioMed Research International, 2014.

[128]. Walsh, C. T., & Moore, B. S. (2019). Enzymatic cascade reactions in biosynthesis. Angewandte Chemie International Edition, 58(21), 6846-6879.

[129]. Hwang, E. T., & Lee, S. (2019). Multienzymatic cascade reactions via enzyme complex by immobilization. ACS Catalysis, 9(5), 4402-4425.

[130]. Tsitkov, S., & Hess, H. (2019). Design principles for a compartmentalized enzyme cascade reaction. ACS Catalysis, 9(3), 2432-2439.